

RESEARCH ARTICLE

PKN2 Is a Dependency of the Mesenchymal-like Cancer Cell State



Shane T. Killarney¹, Gabriel Mesa¹, Rachel Washart¹, Benjamin Mayo², Kerry Dillon¹, Suzanne E. Wardell¹, Madeline Newlin¹, Min Lu¹, Areej Abu Rmaileh¹, Nicky Liu¹, Donald P. McDonnell¹, Ann Marie Pendergast¹, and Kris C. Wood¹

ABSTRACT

Cancer cells exploit a mesenchymal-like transcriptional state (MLS) to survive drug treatments. Although the MLS is well characterized, few therapeutic vulnerabilities targeting this program have been identified. In this study, we systematically identify the dependency network of mesenchymal-like cancers through an analysis of gene essentiality scores in ~800 cancer cell lines, nominating a poorly studied kinase, PKN2, as a top therapeutic target of the MLS. Coessentiality relationships, biochemical experiments, and genomic analyses of patient tumors revealed that PKN2 promotes mesenchymal-like cancer growth through a PKN2-SAV1-TAZ signaling mechanism. Notably, pairing genetic PKN2 inhibition with clinically relevant targeted therapies against EGFR, KRAS, and BRAF suppresses drug resistance by depleting mesenchymal-like drug-tolerant persister cells. These findings provide evidence that PKN2 is a core regulator of the Hippo tumor suppressor pathway and highlight the potential of PKN2 inhibition as a generalizable therapeutic strategy to overcome drug resistance driven by the MLS across cancer contexts.

SIGNIFICANCE: This work identifies PKN2 as a core member of the Hippo signaling pathway, and its inhibition blocks YAP/TAZ-driven tumorigenesis. Furthermore, this study discovers PKN2-TAZ as arguably the most selective dependency of mesenchymal-like cancers and supports specific inhibition of PKN2 as a provocative strategy to overcome drug resistance in diverse cancer contexts.

See related commentary by Shen and Tan, p. 458

INTRODUCTION

The robustness of cancer cell populations in the face of varying environmental selection pressures depends on their ability to engage diverse phenotypic cellular states (1). One way of accessing various cellular states is through “phenotypic plasticity,” a term describing the nongenetic mechanisms cancer cells utilize to alter their biological characteristics through epigenetic, transcriptional, and metabolic reprogramming events (2, 3). A large body of studies has identified the mesenchymal-like state (MLS) as a particularly important, recurrently selected product of phenotypic plasticity that drives tumor progression and therapeutic resistance across diverse cancer contexts (4, 5). Phenotypic features of the MLS include activation of antiapoptotic machinery, altered metabolic demands, decreased cellular proliferation, increased metastatic capacity, and alteration of the tumor microenvironment to avoid immune cell detection (6–8). Taken together, the characteristics of the MLS promote resistance to radiotherapy (9), chemotherapy (10, 11), targeted therapy (12–14), and immunotherapy (15).

Epithelial–mesenchymal plasticity (EMP) is necessary for normal embryologic development and wound healing, but it is exploited by epithelial-derived cancers for tumor development and progression (8, 16–20). Interestingly, nonepithelial

cancers such as melanoma (21), leukemia (22), and neuroendocrine cancers (23–26) also activate mesenchymal-like cellular programs, suggesting that the fitness advantages of this state are generalizable beyond just epithelial cancers. Although the transcription factors and phenotypic mechanisms that drive EMP are well characterized (6–8, 27), few therapeutic interventions targeting the MLS have emerged. GPX4 inhibition was found to induce ferroptosis in mesenchymal-like cancers (28, 29), but pharmacologic options to activate ferroptosis are currently limited (30). Therefore, there is a significant need to identify pharmacologically accessible therapeutic vulnerabilities of the MLS that are generalizable across mesenchymal-like cancer populations.

Here, we discover that the kinase PKN2 is a core regulator of Hippo signaling and is required for mesenchymal-like cancer survival. Additionally, we reveal that PKN2 suppression prevents the MLS-dependent acquisition of resistance to major oncogene-targeted therapies.

RESULTS**PKN2 Is an Understudied Kinase Required for the Survival of Mesenchymal-like Cancers**

In search of genetic dependencies specific to the MLS, we assigned every solid cancer cell line, excluding sarcomas, annotated in the Cancer Dependency Map (DepMap; ref. 31) a score based on its expression of the Hallmark epithelial-mesenchymal transition (EMT) gene signature (Supplementary Fig. S1A; ref. 32). As expected, fibroblast cells uniformly generated the highest EMT scores, highlighting their mesenchymal features (Supplementary Fig. S1B). Conversely, tumor cells from myeloid and lymphoid lineages consistently produced the lowest scores (Supplementary Fig. S1B). Interestingly, solid cancer cell lines exhibited a wide range of EMT

¹Department of Pharmacology and Cancer Biology, Duke University, Durham, North Carolina. ²Department of Molecular Biology, University of Texas Southwestern Medical Center, Dallas, Texas.

Corresponding Author: Kris C. Wood, Duke University, 450 Research Drive, LSRC C134, PO Box 3813, Durham, NC 27710. E-mail: kris.wood@duke.edu
Cancer Discov 2025;15:595–615

doi: 10.1158/2159-8290.CD-24-0928

©2024 American Association for Cancer Research

scores across all cancer lineages (Supplementary Fig. S1A and S1B), which suggests that these cell models faithfully represent the continuum of EMT cell states. Following the exclusion of sarcomas, we performed linear regression analyses in ~800 solid cancer cell lines to assess the correlation coefficient between the EMT score and the gene dependency score for each gene in the genome, derived from genome-wide CRISPR/Cas9 loss-of-function screening data (Fig. 1A; Supplementary Table S1). Genes with the most negative correlation coefficients are more required for the survival of mesenchymal-like cells than epithelial-like cells. Reassuringly, these genes included *GPX4* as a top hit (Fig. 1A), suggesting that this analysis identifies previously validated vulnerabilities of the MLS.

Unexpectedly, although the mRNA expression of many genes is upregulated in MLS-high cell lines, only a small subset of these genes showed differential dependency scores in the same lines. Many of these genes were related to integrin-focal adhesion signaling (*FERMT2*, *JUN*, *ITGAV*, and *VCL*) or the downstream Hippo tumor suppressor signaling pathway (*WWTR1*; Fig. 1B; Supplementary Table S2). Using our ranked list of correlation coefficients (Fig. 1A), we performed GSEA Preranked (33) with Kyoto Encyclopedia of Genes and Genome (KEGG) gene sets, identifying the enrichment of gene sets related to focal adhesion and cytoskeletal regulation among the top dependency pathways enriched in the MLS (Fig. 1C). To ensure our results were not biased by lineages with skewed EMT scores, we repeated our correlation analysis in only non-small cell lung cancer cell lines. We found that the family of focal adhesion genes identified in the pan-cancer analysis was once again the most negatively correlated hits, suggesting that EMT score predicts dependency on these genes even when controlling for cancer lineage (Supplementary Fig. S1C). Together, these data suggest that although hundreds of genes are transcriptionally upregulated in the MLS, a specific network of genes associated with focal adhesion and Hippo tumor suppressor signaling are unique dependencies of mesenchymal-like cancers.

We were particularly interested in *PKN2*, a gene encoding an understudied kinase that scored as the ninth most selective dependency of mesenchymal-like cell lines (Fig. 1A, B, and D). *PKN2* is a Rho effector serine/threonine kinase that becomes activated upon Rho GTPase (RhoA/Rac1) binding to its inhibitory N-terminal domains and is known to be involved in cell cycle regulation and cytoskeletal remodeling (34). Notably, *PKN2* was one of the few mesenchymal-specific dependencies that did not exhibit upregulated mRNA expression in MLS-high cells (Fig. 1B; Supplementary Fig. S1D). Our interest in exploring *PKN2* as a therapeutic target of the MLS is fourfold. First, although no underlying mechanism was identified, *Pkn2* was recently reported to be essential for the expansion of the mesoderm during mouse embryogenesis (35), highlighting the specificity and potency of *Pkn2* dependence in mesenchymal cells *in vivo*. Second, very little is known about *PKN2*'s role in cancer biology and cellular signaling. *PKN2* is known to be involved in cytoskeletal regulation, but it is unclear why mesenchymal-like cancers would require this kinase for survival. Third, *PKN2* can be inhibited by conventional small molecule kinase inhibitors, though no *PKN2*-selective inhibitors that spare other broadly essential kinases exist yet (36, 37). Finally, conditional knockout of

Pkn2 is well tolerated in adult mice, suggesting that future drugs targeting this kinase may exhibit a broad therapeutic window (38).

We began validating *PKN2* as a specific dependency of the MLS using clonogenic growth assays across a panel of cancer cell lines from epithelial or melanocyte lineages with epithelial- or mesenchymal-like transcriptional profiles (Supplementary Fig. S1E). We confirmed the epithelial-like cell lines expressed E-cadherin and showed no evidence of vimentin and the mesenchymal-like cell lines expressed vimentin but not E-cadherin (Supplementary Fig. S1F). Next, we observed the mesenchymal-like cancer cell lines A375 (*BRAF*^{V600E} melanoma), NCI-H2030 [*KRAS*^{G12C} non-small cell lung cancer (NSCLC)], PC3 (castration-resistant prostate adenocarcinoma), and BT549 (triple-negative breast cancer) exhibited markedly diminished growth following genetic *PKN2* ablation with three independent CRISPR/Cas9 single-guide RNAs (sgRNA; Supplementary Fig. S1G), whereas the epithelial-like cancer cell lines 22Rv1 (castration-resistant prostate adenocarcinoma), HCT-15 (*KRAS*^{G12D} colorectal adenocarcinoma), MCF-7 (ER+ breast cancer), and NCI-H1437 (*MEK1*^{Q56P} NSCLC) were minimally affected (Fig. 1E and F). To confirm the mesenchymal-selective nature of *PKN2* dependency, we used two isogenic models: immortalized human mammary epithelial cells (HMLE), which can be induced to undergo EMT by treatment with TGF-β (Fig. 1G; ref. 39), and SKMEL28 *BRAF*^{V600E} mutant melanoma cells, which exhibit hallmarks of the MLS following long-term treatment with a BRAF inhibitor PLX4720 (BRAFi-addicted or BA; Fig. 1H; ref. 40). Interestingly, *PKN2* knockout did not prevent HMLE cells from entering the MLS (Supplementary Fig. S1H), but in each isogenic model, cells became more *PKN2* dependent following induction of the MLS, as defined by loss of E-cadherin and gain of N-cadherin, AXL, and vimentin expression (Fig. 1G and H). Finally, to assess the potency of *PKN2* dependence in mesenchymal cancer cells *in vivo*, we established xenograft tumors from either epithelial-like 22Rv1 [Fig. 1I (left)] or mesenchymal-like PC3 [Fig. 1I (right)] prostate cancer cells in castrated mice, in which each tumor expressed doxycycline-inducible shRNA constructs targeting *PKN2* (or an empty vector control). Consistent with *in vitro* evidence (Supplementary Fig. S1I; Fig. 1E and F), PC3 tumors exhibited *PKN2* dependence *in vivo*, whereas 22Rv1 tumors did not (Fig. 1I). Together, these findings demonstrate that although *PKN2* is dispensable for cellular entry into the MLS, it is selectively required for the survival of cancer cells with mesenchymal features.

Coessentiality Mapping Identifies *PKN2* as a Negative Regulator of the Hippo Tumor Suppressor Pathway

In search of mechanistic insights to explain mesenchymal-specific *PKN2* dependence, we utilized coessentiality mapping to identify genes functionally related to *PKN2* (41). Briefly, genes with highly correlated dependency scores across hundreds of genome-wide essentiality CRISPR/Cas9 screens are considered coessential. Modules of coessential genes have helped assign novel biological functions to poorly characterized proteins (41–43). Recently, a coessentiality interaction

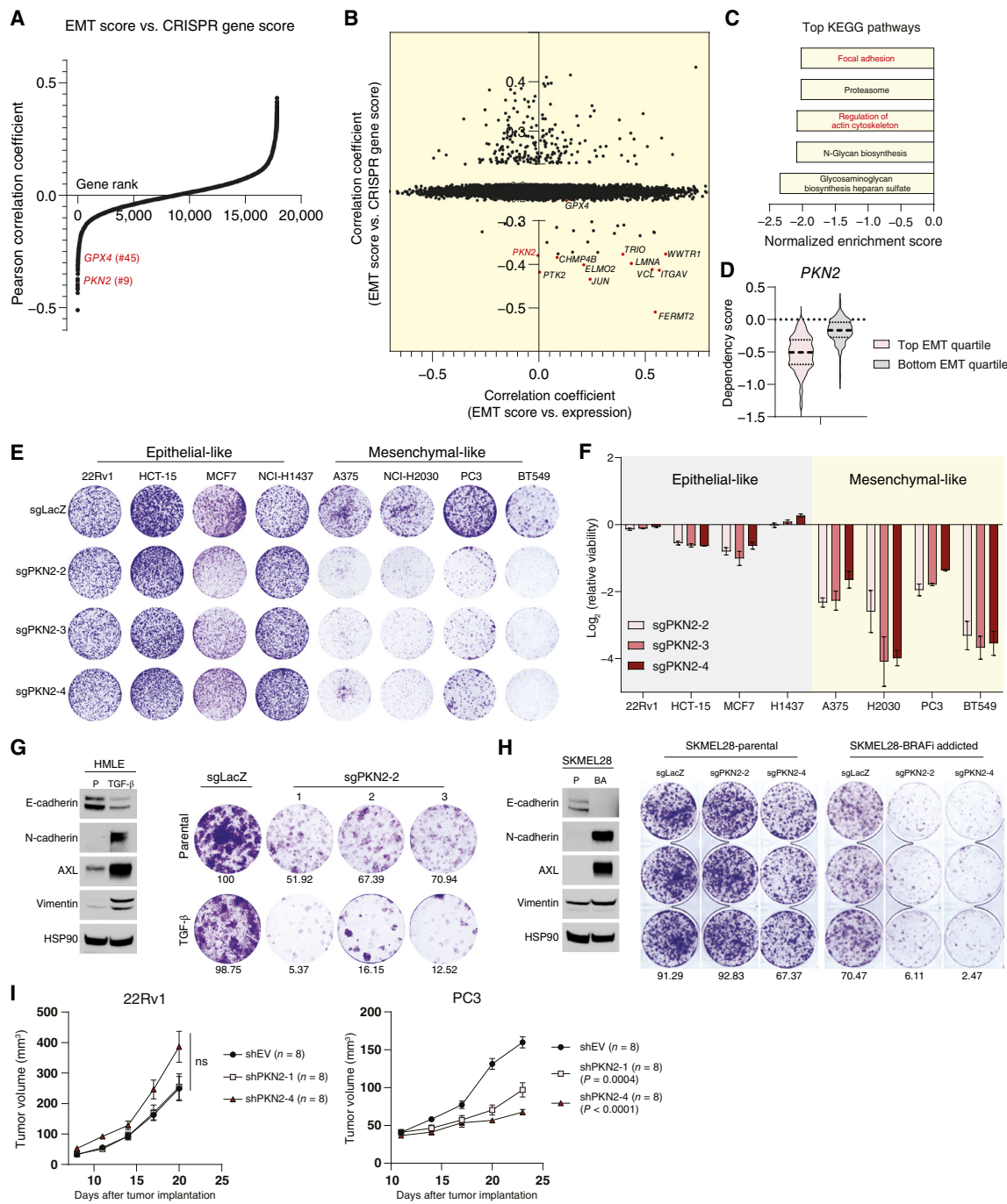


Figure 1. *PKN2* is an understudied kinase required for the survival of mesenchymal-like cancer. **A**, Genome-wide Pearson correlation analysis of gene dependency score (CRISPR gene score) and EMT ssGSEA score in all solid tumor cancer cell lines except sarcoma models. **B**, Scatterplot of correlation coefficients generated from gene dependency score vs. EMT ssGSEA score and mRNA expression vs. EMT ssGSEA score in all solid tumor cancer cell lines except sarcoma models. **C**, Top five enriched KEGG gene sets from a GSEAPrereanked of correlation coefficients in **A**. **D**, *PKN2* gene dependency scores of cell lines in the top 25% or bottom 25% of EMT score. The dashed line represents the median, and the dotted line represents the quartiles. **E**, Clonogenic growth assay of the indicated cell line following CRISPR/Cas9 knockout of *PKN2* with the indicated sgRNA. **F**, Quantitative analysis of data in **E**. The viability of each knockout population was normalized back to its respective LacZ population. **G**, Left, Western blot analysis of the indicated proteins following 5 ng/ml TGF- β treatment for 14 days in HMLE cells. Right, 10,000 parental or TGF- β transformed HMLE cells with knockouts of the indicated genes were seeded in six-well plates and stained with crystal violet dye when the LacZ condition hit confluence. **H**, Left, Western blot analysis of parental or PLX4720-addicted (BA) SKMEL28 cells. Right, 5,000 parental or PLX4720-addicted SKMEL28 cells with the indicated knockouts were stained with crystal violet dye when the LacZ condition hit confluence. **I**, Tumor growth kinetics of 22rv1 and PC3 cells with doxycycline-inducible shRNA against *PKN2* (eight mice per group) were measured on the indicated days. Doxycycline was started once the tumors hit 50–100 mm³, and tumors were measured every 3–4 days. A one-way ANOVA was performed on the last day of measurements with *P* values represented in the panel. **G** and **H**, Quantifications of the percent surface area covered are shown below each clonogenic well. **E**, **G**, and **H**, The data represent three biologically independent experiments ($n = 3$). **F** and **I**, Data are presented as mean \pm SEM.

map was created to identify functional “neighborhoods” of genes through a modified Uniform Manifold Approximation and Projection model (41). We searched for *PKN2* in the coessentiality map and discovered that it clustered with many core members of the Hippo tumor suppressor pathway (44), which was the only pathway significantly enriched upon a Gene Ontology (GO) search of *PKN2*’s “neighborhood” (Fig. 2A).

The Hippo tumor suppressor pathway is an evolutionarily conserved mechanism known to control organ development during embryogenesis, but it is one of the most frequently dysregulated pathways in cancer (45, 46). The primary function of the Hippo pathway is to silence the transcription-activating homologs yes-associated protein 1 (YAP) and WW domain-containing transcription regulator 1 (WWTR1/TAZ; ref. 47). In response to appropriate upstream inputs, mammalian STE20-like protein kinase 1 and 2 (MST1/2) bind to the scaffold protein Salvador family WW domain-containing protein 1 (SAV1), which promotes MST1/2 autophosphorylation and self-activation (48). Once activated, MST1/2 phosphorylates and activates large tumor suppressor kinase 1 and 2 (LATS1/2), which initiates the cytosolic sequestration of YAP and proteasomal degradation of TAZ through phosphorylation events. If Hippo pathway signaling is repressed, YAP and TAZ translocate to the nucleus and associate with DNA-binding proteins, including the TEADs, to stimulate the transcription of oncogenic programs that contribute to cellular proliferation and survival (49).

We corroborated the results from the coessentiality map by finding many core Hippo signaling members, including *WWTR1/TAZ* and *TEAD1*, among top-ranked *PKN2* coessentials in DepMap (Supplementary Fig. S2A). Additionally, using DepMap’s predictability model, we observed that the genomic feature most strongly associated with *PKN2* dependence in a pan-cancer analysis is the mRNA expression level of *CYR61*, a canonical YAP/TAZ target gene (Fig. 2B; ref. 31). Next, we assigned every cell line in DepMap a score corresponding to YAP/TAZ transcriptional activity with single-sample gene set enrichment analysis (ssGSEA) using a 22 target gene signature (45, 50) that only contained three genes that overlapped with the 200-member Hallmark EMT gene set. YAP/TAZ score strongly correlated with *PKN2* dependence (Supplementary Fig. S2B) and EMT score (Supplementary Fig. S2C), implying that the mesenchymal-like cancer cell lines most dependent on *PKN2* also exhibit the highest levels of YAP/TAZ transcriptional activation. Consistent with this observation, levels of canonical YAP/TAZ target genes were higher in isogenic HMLE and SKMEL28 models that underwent EMT (Supplementary Fig. S2D). Interestingly, our correlation analysis revealed that mesenchymal-like cancer cells were specifically dependent on *TAZ* (hit #11) for survival but not *YAP* (hit #6502; Supplementary Fig. S2E). We validated that *TAZ*, but not *YAP*, is a mesenchymal-specific dependency in the isogenic SKMEL28 parental (epithelial-like) and SK28-BA (mesenchymal-like) model (Supplementary Fig. S2F). Finally, we observed that *PKN2-TAZ* dependence poorly correlates with *YAP* dependence across all lineages (Supplementary Fig. S2G), suggesting that cancer lineages may become dependent on *PKN2-TAZ* and *YAP* through different molecular mechanisms.

To interrogate if *PKN2* regulates YAP/TAZ signaling, we knocked out *PKN2* with four independent sgRNAs in SKMEL28 melanoma cells. Genetic *PKN2* ablation resulted in mRNA suppression of a panel of the canonical YAP/TAZ target genes *ANKRD1*, *CTGF*, and *CYR61* (Fig. 2C) and decreased TAZ protein expression (Fig. 2D). To determine whether *PKN2*’s modulation of YAP/TAZ occurs through the canonical Hippo pathway, we knocked out *PKN2* in 293FT cells, which resulted in an increase in phosphorylation of *LATS1^{T1079}* and *YAP^{S397}* and downregulation of total TAZ levels, all of which are consistent with Hippo pathway activation and downstream suppression of YAP/TAZ target gene expression (Fig. 2E). We corroborated that *PKN2* loss resulted in YAP/TAZ inactivation in three additional mesenchymal-like cancer cell line models (Fig. 2F). Reciprocally, ectopic expression of a constitutively active *PKN2* truncation mutant ($\Delta 642$) that lacks its autoinhibitory N-terminal Rho-binding domains, HR1a-c (51), results in significantly elevated TAZ protein expression (Fig. 2G). This effect requires *PKN2* kinase activity, as expression of the $\Delta 642$ construct with a point mutation in the catalytic lysine (K686A) prevented TAZ protein upregulation (Fig. 2G). Consistent with the hypothesis that *PKN2* regulates YAP/TAZ through the canonical Hippo pathway, *PKN2^{\Delta 642}* expression in 293FT cells decreased *LATS1^{T1079}*, *YAP^{S127}*, and *YAP^{S397}* phosphorylation, an effect that depends on *PKN2* kinase activity (Fig. 2H). Similar effects were observed on the expression of canonical YAP/TAZ target genes, including *CYR61* (Fig. 2I). Together, these findings establish that activated *PKN2* is a necessary and sufficient positive regulator of oncogenic YAP/TAZ activity that antagonizes the Hippo signaling pathway.

A Hippo Pathway-Resistant TAZ Mutant Rescues *PKN2* Dependency

Given that *PKN2* loss leads to suppression of YAP/TAZ target gene expression in association with activation of the Hippo signaling pathway, coupled with the fact that mesenchymal-like tumors utilize TAZ signaling as a core survival program, we hypothesized that *PKN2* dependence in mesenchymal-like cancers could be rescued through the expression of a Hippo-resistant TAZ mutant. We expressed wild-type TAZ (*TAZ^{WT}*) and a TAZ construct with its four canonical LATS1/2 regulatory phosphosites (S66, S89, S117, and S311) mutated to alanine (*TAZ^{S4A}*; ref. 52) in SK28-BA cells and validated that both constructs showed significantly increased TAZ target gene expression (Supplementary Fig. S2H). We observed that the forced expression of *TAZ^{S4A}*, but not *TAZ^{WT}*, rescued the suppression of the TAZ target gene *ANKRD1* (Fig. 2J) and *PKN2* dependence (Fig. 2K) following *PKN2* knockout in SK28-BAs, consistent with the concept of Hippo-dependent TAZ regulation by *PKN2*. We confirmed this rescue result in two additional *PKN2*-dependent mesenchymal-like cancer cell lines (BT549 and NCI-H2030; Supplementary Fig. S2I and S2L). Together, these findings support a model wherein mesenchymal-like cancer cells become addicted to *PKN2*’s repressive effects on Hippo signaling and resultant downstream TAZ activation, for their survival and proliferation.

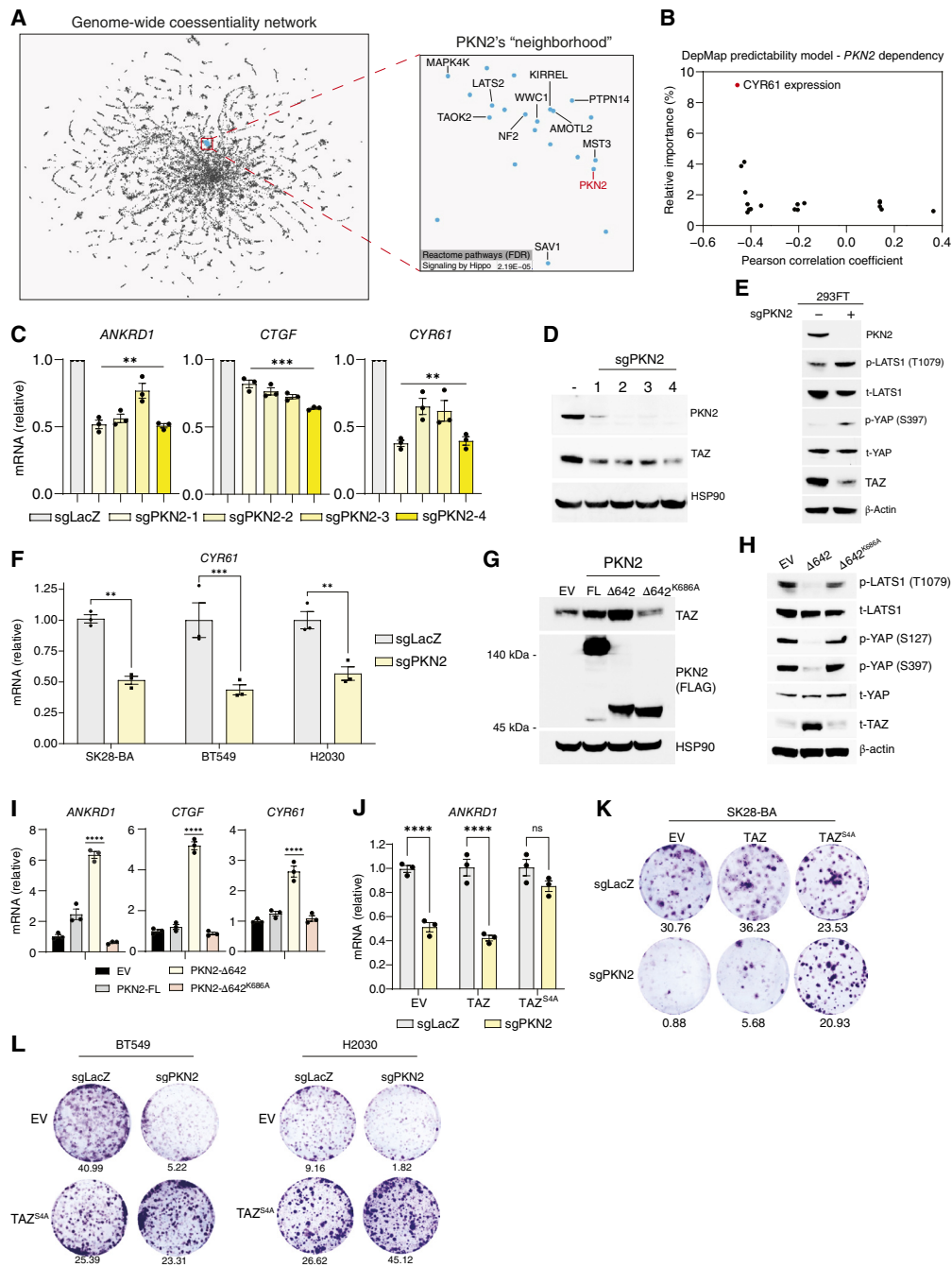


Figure 2. Coessentiality mapping identifies PKN2 as a negative regulator of the Hippo tumor suppressor pathway. **A**, Identification of PKN2's coessentiality neighborhood on coessentiality.net. All Hippo pathway-related members were annotated. **B**, Representation of the DepMap PKN2 dependence predictability model using CoreOmics features. **C**, RT-qPCR of ANKRD1, CTGF, and CYR61 48 hours after knockout of PKN2 in SKMEL28 cells with the PKN2 sgRNAs 1–4. **D**, Western blot analysis of the indicated proteins 48 hours after knockout of PKN2 with sgRNAs 1–4. **E**, Western blot analysis of the indicated proteins in 293FT cells following PKN2 knockout with sgPKN2-2. **F**, RT-qPCR of CYR61 in SKMEL28 PLX4720-addicted (SK28-BA), BT549, and NCI-H2030 cells with knockout of LacZ or PKN2 with sgPKN2-2. **G**, Overexpression of empty vector (EV), full-length (FL) PKN2, 643–948 amino acids (Δ642) PKN2, and Δ642 PKN2 with a K686A mutation (Δ642^{K686A}) in 293FTs for 24 hours. Western blot analysis was performed on the cell pellets for the indicated proteins. **H**, Overexpression of EV or the indicated PKN2 variants in 293FTs for 24 hours before immunoblotting. **I**, Overexpression of EV or the indicated PKN2 variants in 293FTs for 48 hours. RT-qPCR was performed on the cell pellets to measure the relative mRNA of the indicated genes. **J**, Knockout of PKN2 in SK28-BA cells stably overexpressing EV, TAZ (WT), and TAZ^{S4A} with sgPKN2-2. RT-qPCR was performed on the cell pellets for ANKRD1. **K**, SK28-BA cells stably expressing EV, TAZ (WT), or TAZ^{S4A} had PKN2 (sgPKN2-2) knocked out before being seeded into six-well plates at 5,000 cells per well. Crystal violet staining was performed when the EV-LacZ population hit confluence. **L**, BT549 and NCI-H2030 cells stably expressing EV or TAZ^{S4A} had PKN2 (sgPKN2-2) knocked out before being seeded into six-well plates at 5,000 cells per well. Crystal violet staining was performed when the EV-LacZ population hit confluence. **C**, **F**, and **I-J**, One-way ANOVA was performed. *P* values are defined as nonsignificant (ns) > 0.05; **, *P* < 0.01; ***, *P* < 0.001; ****, *P* < 0.0001. **D**, **E**, **G**, **H**, **K**, and **L**, The data represent three biologically independent experiments (*n* = 3). **K** and **L**, Quantifications of the percent surface area covered shown below each clonogenic well. **C**, **F**, **I**, and **J**, Data are presented as mean ± SEM.

PKN2 Directly Modulates the Hippo Pathway through Phosphorylation of SAV1

To define the molecular mechanism through which PKN2 regulates the Hippo pathway, we performed quantitative phosphoproteomics to identify serine and threonine residues differentially phosphorylated in 293FT cells expressing either PKN2^{Δ642} (constitutively active) or PKN2^{Δ642-K868A} (kinase dead; Fig. 3A; Supplementary Table S3). Reassuringly, we observed strong enrichment in phosphorylation of predicted PKN2 substrates, derived from a recently published serine/threonine substrate atlas (53), in PKN2^{Δ642} expressing cells [Fig. 3B (left)]. An unbiased kinase enrichment analysis (53) of the phosphoproteomics dataset revealed that predicted PKN2 substrates were the most differentially enriched phosphosites in the PKN2^{Δ642} condition (Supplementary Fig. S3A). Consistent with PKN2's putative regulation of the Hippo pathway, we observed that substrates of MST1/2 were among the top depleted phosphosites in the PKN2^{Δ642} condition (Supplementary Fig. S3B). Diminished MST1/2 kinase activity in PKN2^{Δ642} expressing cells was further confirmed through mass spectrometry analysis and immunoblotting that showed a reduction of canonical MST1/2 phosphosites LATS1^{S872}, LATS1^{S909}, and LATS1/2^{T1079} (Fig. 2H; Supplementary Fig. S3C). These data together suggest that direct PKN2 substrates are enriched in the phosphoproteomic dataset and that PKN2 regulates the Hippo pathway at or above the level of MST1/2.

We next created a refined list of candidate PKN2-specific substrates by applying filters to select substrates that (i) are predicted, direct PKN2 sites from the serine/threonine substrate atlas (51) and (ii) exhibit a >2-fold change in abundance at $P < 0.05$, in cells expressing PKN2^{Δ642} relative to PKN2^{Δ642-K868A} in the phosphoproteomic dataset. Using these strict criteria, we generated a list of 129 unique candidate PKN2 substrates [Fig. 3B (right); Supplementary Table S4]. Although we observed many significant differences in the phosphorylation of Hippo signaling pathway members (54) in PKN2^{Δ642} expressing cells (Supplementary Fig. S3D), SAV1^{S90} was the only core Hippo pathway phosphorylation site meeting both the above selection criteria [Fig. 3B (right)]. To further interrogate this finding, we searched for PKN2 interactors in a recent large-scale, systematic kinobead competition and correlation analysis (kiCCA) of all human kinases (55) and found it was predicted to interact with multiple regulators of Hippo signaling, including SAV1 (Supplementary Fig. S3E, red genes). Furthermore, we attempted to predict an Alpha-fold3 (56) model of activated PKN2 (phospho-T816) with SAV1 (phospho-S90). The resultant PKN2:SAV1 heterodimer prediction contains multiple interaction surfaces, with phospho-S90 located proximal to the PKN2 kinase activity site (Fig. 3C), which suggests that PKN2 may directly interact with SAV1 in a manner that makes S90 accessible to PKN2's kinase domain. Biochemically, the SAV1^{S90} sequence motif (IMRRES*NRLSA) is primed for phosphorylation by basophilic kinases based on the arginine residues at the -3, -2, and +2 positions (53). A Protein Blast (57) search of the human SAV1^{S90} peptide sequence revealed that SAV1^{S90} is evolutionarily conserved throughout vertebrates, which implies it may play an essential role in the regulation of vertebrate SAV1 function (Supplementary Fig. S3F). Together, these data nominate PKN2's

phosphorylation of SAV1^{S90}, which lies directly upstream of MST1/2, as a candidate mechanism of Hippo pathway inhibition.

We first confirmed that HA affinity-tagged SAV1 coimmunoprecipitates with activated PKN2^{Δ642} but not inactive full-length PKN2 in 293FT cells (Supplementary Fig. S3G). Next, we examined the serine/threonine substrate atlas (53) and found that PKN2 is a top-ranked kinase for two SAV1 sites, S90 and S36 (Supplementary Fig. S3H). Although a significant change in SAV1^{S90} phosphorylation was observed in the phosphoproteomics dataset (Supplementary Fig. S3H), no SAV1^{S36} phosphopeptides were detected. To determine if PKN2 phosphorylates SAV1 in cells, we coexpressed active ($\Delta 642$) or dead ($\Delta 642-K868A$) PKN2 with wild-type or mutated SAV1 in 293FTs, then resolved lysates using a phostag gel. We observed a robust laddering pattern (phosphorylation) of SAV1 in PKN2-activated cells that was lost in cells expressing SAV1^{S90A} but not SAV1^{S36A} (Fig. 3D). Using SAV1^{WT} and SAV1^{S90A} as substrates, we performed an *in vitro* kinase assay with purified PKN2 and assessed phosphorylation of SAV1 with a phospho-serine antibody that detects RRXS* motifs like the one found at SAV1^{S90}. Following incubation with activated PKN2, SAV1^{WT} showed a pronounced p-serine (RRXS*) signal that was ablated in the SAV1^{S90} condition (Fig. 3E). Together, these data demonstrate that PKN2 directly phosphorylates SAV1^{S90}, making it the only known kinase to phosphorylate this site in a cell-based system.

Next, we set out to understand the signaling impact of PKN2's phosphorylation of SAV1^{S90} on the Hippo pathway. Firstly, expression of SAV1 in the presence of MST2 and PKN2^{Δ642} led to phosphorylation of an RRXS* motif at SAV1's expected molecular weight and disruption of the agonistic Hippo pathway SAV1-MST2 interaction (Fig. 3F). We next generated stable SAV1 knockout 293FT (SAV1^{-/-}) cells, validated protein loss via immunoblotting (Fig. 3G), and confirmed functional loss of SAV1 through TAZ protein stabilization (Fig. 3G). We then knocked out endogenous PKN2 in control (SAV1^{WT}) and SAV1^{-/-} cells, observing the loss of TAZ protein levels in only SAV1^{WT} cells (Fig. 3G), suggesting that SAV1 expression is required for PKN2-dependent regulation of TAZ. Next, we expressed active PKN2 in 293FT cells harboring endogenous SAV1, SAV1 knockout, or SAV1 knockout with rescued, ectopic WT SAV1 (Fig. 3H). This analysis once again revealed that PKN2's ability to stabilize TAZ protein levels depends upon the presence of SAV1. Finally, PKN2-dependent stabilization of TAZ and expression of the TAZ target gene ANKRD1 are reversible through the expression of the nonphosphorylatable SAV1^{S90A} mutant (Fig. 3I and J). Together, these results demonstrate that PKN2 inhibits the Hippo pathway, leading to downstream YAP/TAZ activation through its phosphorylation of SAV1^{S90}.

The PKN2 Substrate Signature Is Enriched in Patients with YAP/TAZ-High Tumors

To understand if the MLS promotes the activation of PKN2 and phosphorylation of SAV1, we induced EMT with our previously validated HMLE system (Supplementary Fig. S1H). As the HMLE cells transitioned to the mesenchymal-like state, phosphorylation of PKN2^{T816} was increased (Fig. 3K).

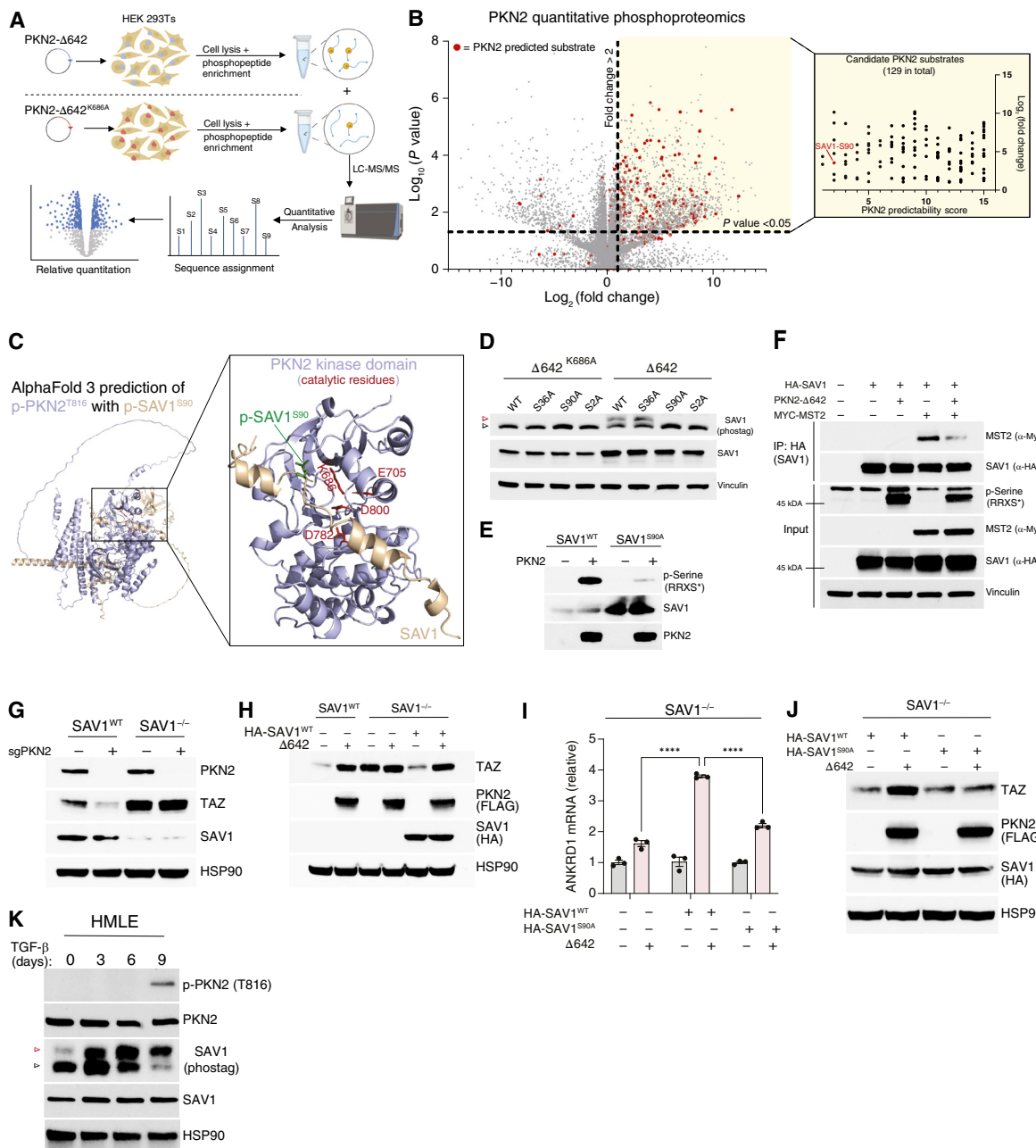


Figure 3. PKN2 directly modulates the Hippo pathway through the phosphorylation of SAV1. **A**, Schematic of quantitative phosphoproteomics experimental design created with Biorender.com. **B**, Left, Volcano plot of experimental results from the experiment depicted in **A**. PKN2 predicted substrates are all substrates in which PKN2 was a top 15-ranked kinase in the serine/threonine substrate atlas (53). Right, The candidate PKN2 substrate signature: Substrates (i) were a predicted top 15 substrate for PKN2 and (ii) showed a fold change >2 in PKN2-expressing cells at $P < 0.05$. The predictability score is the rank of PKN2 for the specified substrate from the atlas of serine/threonine substrates. **C**, AlphaFold 3 prediction of interaction between full-length PKN2 (phospho-T816) with full-length SAV1 (phospho-S90). The PKN2 kinase domain is highlighted with key catalytic residues shown in red. The SAV1-S90 residue is highlighted in green. **D**, Specified SAV1 mutants were coexpressed with PKN2- Δ 642 and PKN2- Δ 642^{K686A} for 24 hours at a 1:1 ratio in 293FT cells. The resulting lysates were separated in polyacrylamide gels with or without phos-tag and blotted for the stated proteins. The red arrow highlights a p-SAV1^{S90} band and the black arrow highlights SAV1 (unphosphorylated). **E**, In vitro kinase assay of purified PKN2 with HA-SAV1^{WT} or HA-SAV1^{S90A} substrates. The reaction results were subjected to immunoblotting for the specified proteins. **F**, HA-SAV1^{WT} was expressed alone or in the specified combinations with PKN2- Δ 642^{K686A} and MYC-MST2 in 293FT for 24 hours before immunoprecipitation with HA beads. Input and IP lysates were subjected to immunoblotting. **G**, Control (SAV1^{WT}) and SAV1 knockout (SAV1^{-/-}) 293FT cells were transduced with CRISPR/Cas9 virus containing sgLacZ or sgPKN2-2. Following selection, the cells were seeded at equal density for 48 hours before immunoblotting for the specified proteins. **H**, SAV1^{WT} and SAV1^{-/-} 293FT cells were transfected with the indicated plasmid combinations at a 1:1 ratio for 24 hours before immunoblotting. **I**, SAV1^{-/-} 293FT cells were transfected to express SAV1^{WT} or SAV1^{S90A} for 24 hours before transfection with PKN2- Δ 642 at a 4:1 ratio. RT-qPCR was performed 24 hours after Δ 642 transfection. One-way ANOVA was performed. P values are defined as ****, $P < 0.0001$. Data are presented as mean \pm SEM. **J**, SAV1^{-/-} 293FT cells were transfected to express SAV1^{WT} or SAV1^{S90A} and PKN2- Δ 642 at a 4:1 ratio for 24 hours before immunoblotting. **K**, HMEL cells were treated with 5 ng/mL TGF- β for the indicated times. Immunoblotting was performed for the specified proteins.

[$\text{PKN2}^{\text{T816}}$ is the site within PKN2's activation loop that PDK1 phosphorylates to promote its kinase activity (34, 51)]. Additionally, induction of EMT led to phosphorylation of SAV1, as demonstrated by its slowed progression through a phostag gel (Fig. 3K). These data correspond to the activation of YAP/TAZ signaling previously observed in this model (Supplementary Fig. S1D).

To investigate if the MLS is associated with PKN2 kinase activity and SAV1 phosphorylation in patient tumors, we utilized data from the National Cancer Institute's Clinical Proteomic Tumor Analysis Consortium (CPTAC), which recently characterized transcriptomic, proteomic, and phosphoproteomic features of >1,100 human patient tumors from 11 cancer lineages to allow for pan-cancer analysis (58–60). Based on PKN2's ability to inactivate Hippo signaling, we sought to determine whether PKN2 is differentially activated in tumor samples with high YAP/TAZ target gene expression. To do this, we first assigned every patient in the database a YAP/TAZ transcriptional score using ssGSEA and then correlated each patient's YAP/TAZ score against the abundance of every protein in the CPTAC proteomics dataset using a simple linear regression model (Fig. 4A; Supplementary Table S5). A positive correlation coefficient from this analysis indicates enhanced protein expression in tumors with high YAP/TAZ transcriptional activity. Reassuringly, we found that proteins representing multiple top-ranked mesenchymal-specific dependencies (ILK, VCL, TLN1, FERMT2, and WWTR1/TAZ) and the YAP/TAZ target CYR61 were among the top positive correlates (Supplementary Table S5). Strikingly, an unbiased GSEAPreranked analysis of correlation coefficients using the Hallmark gene sets (32) revealed that the EMT gene set was the most positively enriched signature from this analysis (Supplementary Fig. S3I), confirming our previous result that mesenchymal-like cancers are significantly enriched for high YAP/TAZ transcriptional activity (Supplementary Fig. S2C).

Next, we identified the serine/threonine kinases most differentially upregulated (DAPK3, NEK7, MST1, AKT3, and ROCK2) and downregulated (SRPK1, VRK1, CDK12, CDK9, and TTK) at the protein level in YAP/TAZ-high tumors based on their correlation coefficients (Fig. 4A; Supplementary Fig. S3J). PKN2 protein abundance did not correlate with YAP/TAZ transcriptional activity (Fig. 4A; Supplementary Fig. S3J), which aligns with our previous observations (Fig. 1B; Supplementary Fig. S1D). Separately, we correlated YAP/TAZ score against all phospho-substrates represented in the CPTAC pan-cancer dataset (Supplementary Table S6) and found four n-terminal SAV1 phosphosites, including SAV1^{S90}, were significant positive correlates of YAP/TAZ score (Supplementary Fig. S3K). Using kinase substrate signatures from the serine/threonine substrate atlas (Supplementary Table S7; ref. 53), we assessed how predicted kinase substrate signatures correlated with YAP/TAZ activity. As a positive control, we observed that 5/5 kinases predicted to be strongly upregulated at the protein level in YAP/TAZ-high tumors showed corresponding positive enrichment of their substrate signatures (Fig. 4B). Reciprocally, 4/5 kinases strongly downregulated at the protein level in YAP/TAZ-high tumors showed corresponding downregulation of their predicted kinase activities in this setting (Fig. 4B). Interestingly, the PKN2 substrate signature that we experimentally validated to be highly specific to PKN2 kinase activity (Fig. 3B;

Supplementary Fig. S3A) was significantly enriched in the positive correlates (Fig. 4B and C). These data suggest that although PKN2 protein levels are not elevated, its kinase substrate signature is enriched to a degree equal to the most upregulated kinases in YAP/TAZ-high tumors (Fig. 4D).

Through isogenic experimental models and analysis of proteogenomic profiles of pan-cancer tumors from patients, these data support a mechanistic model in which induction of the mesenchymal-like state leads to posttranslational activation of PKN2 and resultant phosphorylation of SAV1 to antagonize Hippo signaling and promote the oncogenic activation of YAP/TAZ (Fig. 4E).

Drug-Tolerant Persister Cells Require PKN2 for Survival

Cancer cells resistant to oncogene-targeted therapies such as EGFR, KRAS, and BRAF inhibitors emerge from the reservoir of residual disease cells that survive upfront treatments. These residual cells often exhibit a nongenetic and reversible "drug-tolerant persister" (DTP) phenotype, and its hallmark features include reduced proliferation, multidrug resistance, and vulnerability to ferroptosis (61, 62). Notably, a growing body of work has demonstrated that residual or DTP cells from diverse tumor lineages surviving treatment with EGFR, KRAS, and BRAF inhibitors also exhibit mesenchymal-like features and converge on YAP/TAZ signaling for their survival (63–67).

To understand if PKN2 is a specific vulnerability of the DTP state, we first validated that a panel of EGFR (PC9, MGH134, HCC827, and HCC4006), KRAS (NCI-H358 and NCI-H23), and BRAF (SKMEL28 and RKO) mutant models exhibit mesenchymal features and elevated YAP/TAZ signaling following the induction of the residual disease state with oncogene-targeted therapy (Fig. 5A; refs. 66–70). DepMap gene expression profiling revealed that 6/7 profiled cell lines were at or below the 50th percentile for baseline EMT score compared with all solid tumor cell lines (Supplementary Fig. S4A). Additionally, CRISPR screening data from all four of the lines from this list screened by DepMap revealed low baseline PKN2 dependence, corresponding to the bottom half of solid tumor cell lines (Supplementary Fig. S4B).

We treated PC9-tet-on-sgRNA cells for 3 days with the third-generation EGFR inhibitor osimertinib to generate the DTP state before inducing the knockout of PKN2 with doxycycline (Fig. 5B). On day 9 of treatment (day 6 post-PKN2 knockout), the control residual cells demonstrated (i) increased phosphorylation of $\text{PKN2}^{\text{T816}}$ (Fig. 5C), (ii) elevated levels of the apoptotic cell death markers cleaved caspase 3 (Fig. 5C) and annexin V⁺/PI⁺ staining (Fig. 5D), (iii) an activated YAP/TAZ transcriptional signature (Fig. 5E), and (iv) cell cycle arrest (Fig. 5F) when compared with parental PC9 cells. Importantly, PKN2 knockout potentiated apoptotic cell death (Fig. 5C and D) and blunted YAP/TAZ target gene expression (Fig. 5E) in the PC9 DTP cells. Finally, PKN2 knockout blocked long-term re-entry into the cell cycle (Fig. 5F) seen in control drug-tolerant expanding persisters (DTEP). These findings were corroborated and expanded upon in other DTP models, which demonstrated increased phosphorylation of $\text{PKN2}^{\text{T816}}$ and TAZ protein stabilization (Fig. 5G), elevated phosphorylation of SAV1 (Fig. 5H), and significant reduction of YAP/TAZ target gene expression by PKN2 knockout (Fig. 5I).

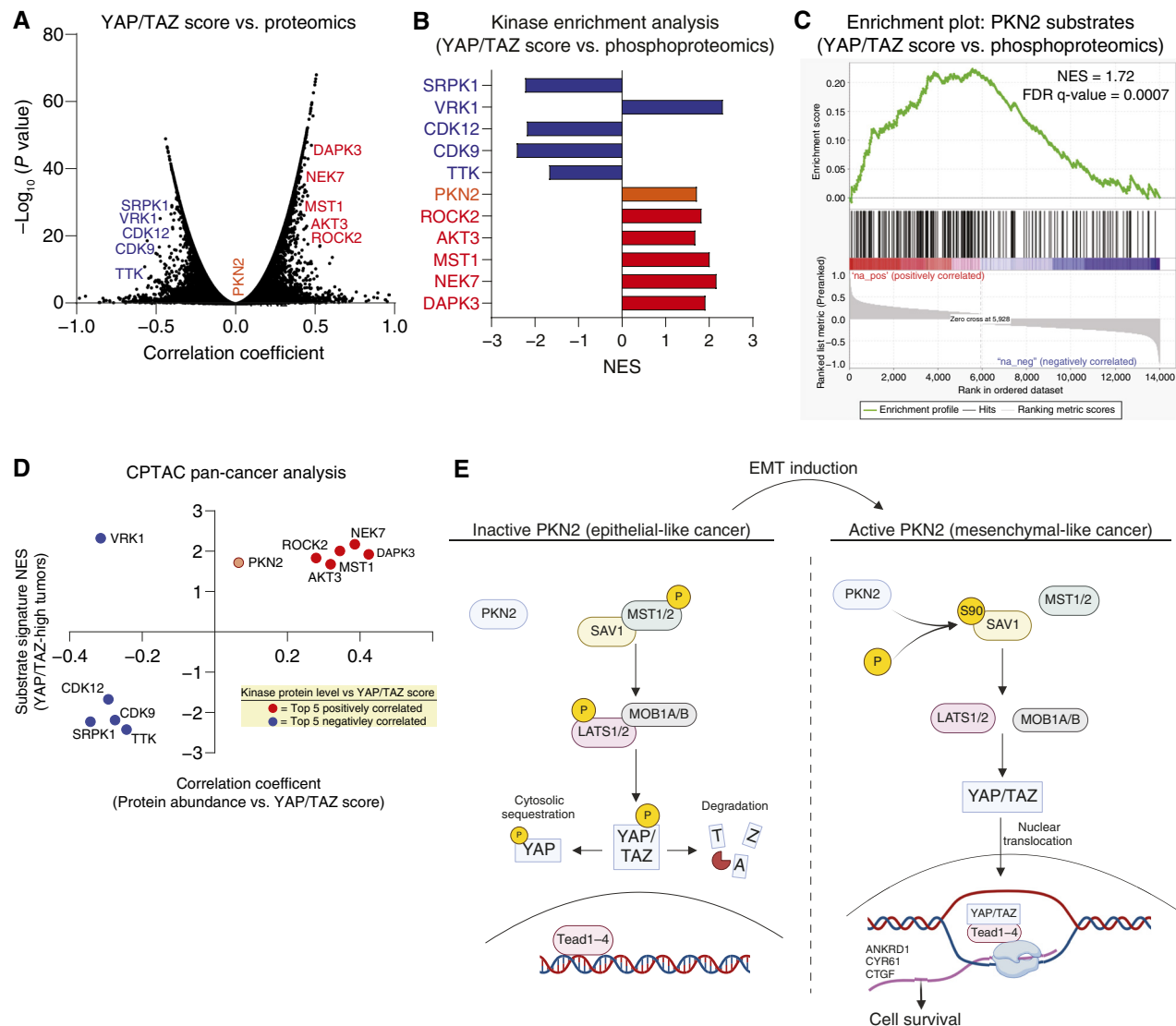


Figure 4. The PKN2 substrate signature is enriched in YAP/TAZ-high patient tumors. **A**, Statistical results of linear regression models comparing YAP/TAZ ssGSEA score vs. protein abundance (Proteomics) across all patient samples in CPTAC. **B**, GSEApreranked analysis of kinase substrate signatures was performed using the ranked correlation coefficients from the YAP/TAZ score vs. phosphoproteomics dataset. Normalized enrichment scores (NES) for each kinase from this analysis are shown. **C**, Running enrichment plot of the PKN2 substrate signature following a GSEApreranked analysis of correlation coefficients from the YAP/TAZ score vs. phosphoproteomics dataset. **D**, X-axis: Correlation coefficient plot resulting from a linear regression model of protein abundance vs. YAP/TAZ transcriptional score in all CPTAC patient tumors. Y-axis: GSEApreranked normalized enrichment score of each of the specified kinase's substrate signature from the phosphoproteomics vs. YAP/TAZ transcriptional score ranked correlational coefficient list. **E**, Schematic of PKN2's regulation of Hippo signaling created with Biorender.com.

We introduced inducible CRISPR/Cas9 systems into the PC9 [CRISPR-SWITCH (71)] and H23-Cas9 (Tet-on-sgRNA) models and validated their ability to knockout *PKN2* upon appropriate treatment (Supplementary Fig. S4C and S4D). We treated these models with high-dose oncogene-targeted therapy and induced *PKN2* knockout for 9 days before withdrawing the drug and allowing the residual cells to resume growth [Fig. 5J (left)]. In both models, *PKN2* knockout resulted in markedly diminished survival and fitness of residual cells, demonstrated by the lack of outgrowth in *PKN2* knockout DTP cells compared with the control DTP cells [Fig. 5J (right)].

These data support the idea that after selecting a residual or DTP tumor state, *PKN2* becomes activated, stimulates YAP/TAZ transcription, and is required for survival.

PKN2 Inhibition Suppresses Resistance to Oncogene-Targeted Therapies

The fact that residual or DTP tumor cells require *PKN2* for survival suggests that concomitant inhibition of *PKN2* and driver oncoproteins should yield deeper and more durable therapeutic responses. Indeed, we observed that upfront *PKN2* knockout led to 3 to 4-fold deeper responses to matched oncogene-targeted therapies in H23, PC9, and MGH134

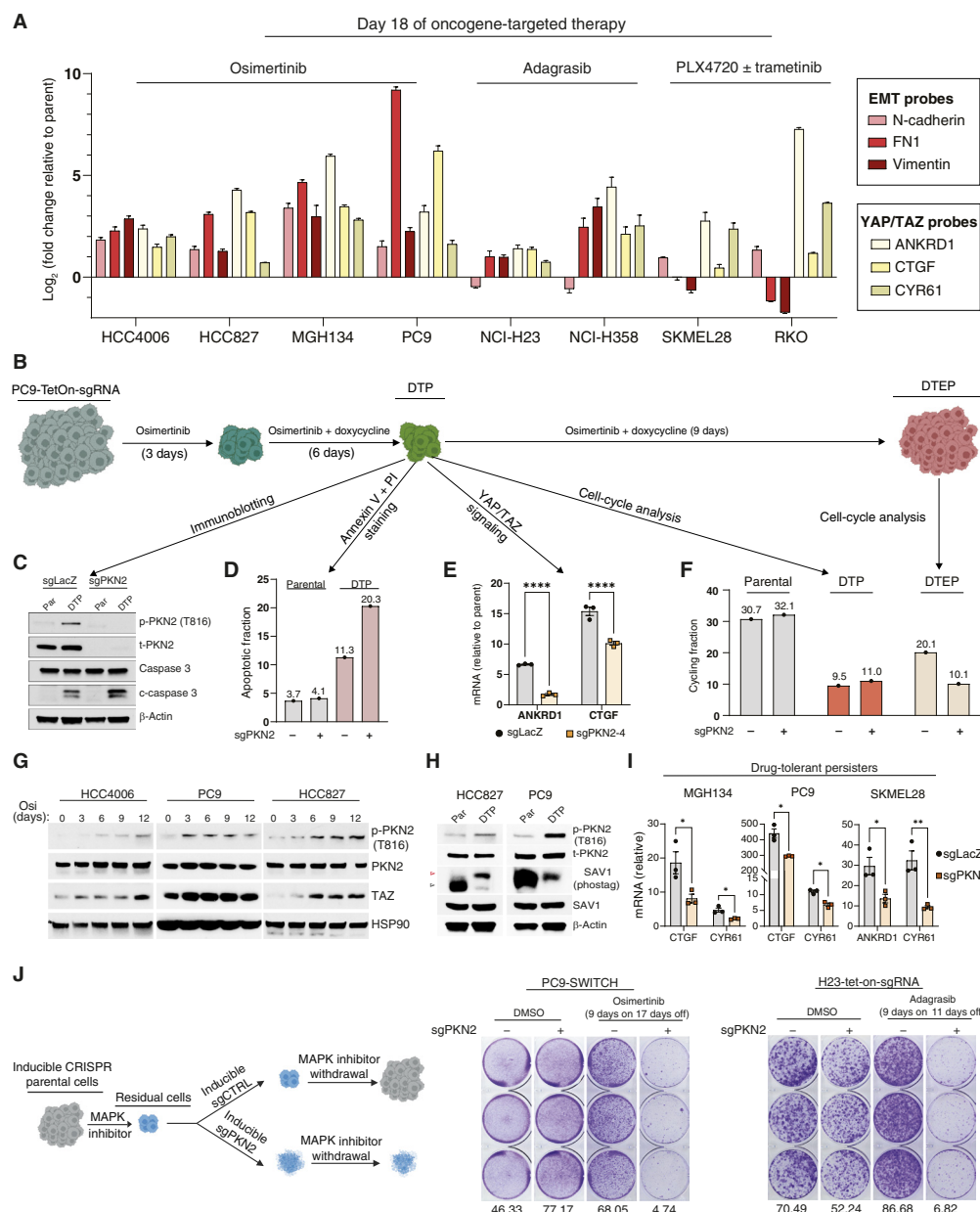


Figure 5. Drug-tolerant persisters require PKN2 for survival. **A**, RT-qPCR of the indicated cell lines on day 18 of oncogene-targeted therapy. HCC4006, HCC827, MGH134, and PC9 cells were treated with 500 nmol/L osimertinib. NCI-H23s were treated with 1 μmol/L adagrasib. NCI-H358s were treated with 50 nmol/L adagrasib. SKMEL28s were treated with 3 μmol/L PLX4720. RKOs were treated with 1 μmol/L PLX4720 and 100 nmol/L trametinib. All drugs were refreshed every 72 hours. **B**, Schematic of experimental design for **C–F** created with BioRender.com. PC9-tet-on-sgRNA cells containing sgRNAs against sgLacZ or sgPKN2 were treated with DMSO or 500 nmol/L osimertinib for 72 hours before switching the media to DMSO + 500 ng/mL doxycycline or 500 nmol/L osimertinib + 500 ng/mL doxycycline for an additional 9 days. The resultant cell population was subject to **(C)**, immunoblotting for the specified proteins and **(D)** annexin V and propidium iodide (PI) cell surface flow cytometry. The apoptotic fraction was the percentage of cells that stained positive for annexin V+/PI-. **(E)**, RT-qPCR for the indicated gene transcripts, and **(F)**, Flow cytometry for cell cycle analysis with Hoechst 3342 in parental, DTP, and DTEP. The cycling fraction was the percentage of cells in the S-M-G₂ phase. **G**, HCC4006, PC9, and HCC827 cells treated with 500-nmol/L osimertinib (Osi) for the indicated time points. Drug was refreshed every 72 hours. Immunoblotting for the specified protein was performed on the resultant cell lysates. **H**, HCC827 and PC9 cells were treated with 500-nmol/L osimertinib for 12 days to induce a DTP state. Parental (Par) cells treated with DMSO were used as controls. Drug was refreshed every 72 hours. Immunoblotting for the specified proteins was performed with a red arrow demonstrating phosphorylated SAV1. **I**, RT-qPCR was performed on sgLacZ or sgPKN2 (500 nmol/L osimertinib), PC9 (500 nmol/L osimertinib), and SKMEL28 (3 μmol/L PLX4720) cells following 6 days of treatment with their oncogene-targeted therapy. Drug was refreshed every 72 hours. mRNA was normalized back to parental control cells treated with DMSO. **J**, Left, Experimental schematic created with Biorender.com. Middle, 50,000 PC9-SWITCH-sgCTRL or PC9-SWITCH-sgPKN2-2 cells were seeded in six-well plates and treated with 500 nmol/L osimertinib and DMSO or 100 nmol/L 4-OHT for 9 days before drug withdrawal. Right, 150,000 Tet-On-sgRNA H23-sgCTRL or H23-sgPKN2 cells were seeded in six-well plates and treated with 500 ng/mL doxycycline in the presence of 3 μmol/L adagrasib or DMSO for 9 days before drug withdrawal. Crystal violet staining was performed when sgCTRL cells hit confluence. All drugs were refreshed every 72 hours. **G** and **H**, The data represent three biologically independent experiments ($n = 3$). **E** and **I**, Two-tailed unpaired t test P values are defined as *, $P < 0.05$; **, $P < 0.01$; ***, $P < 0.0001$. Data are presented as mean \pm SEM.

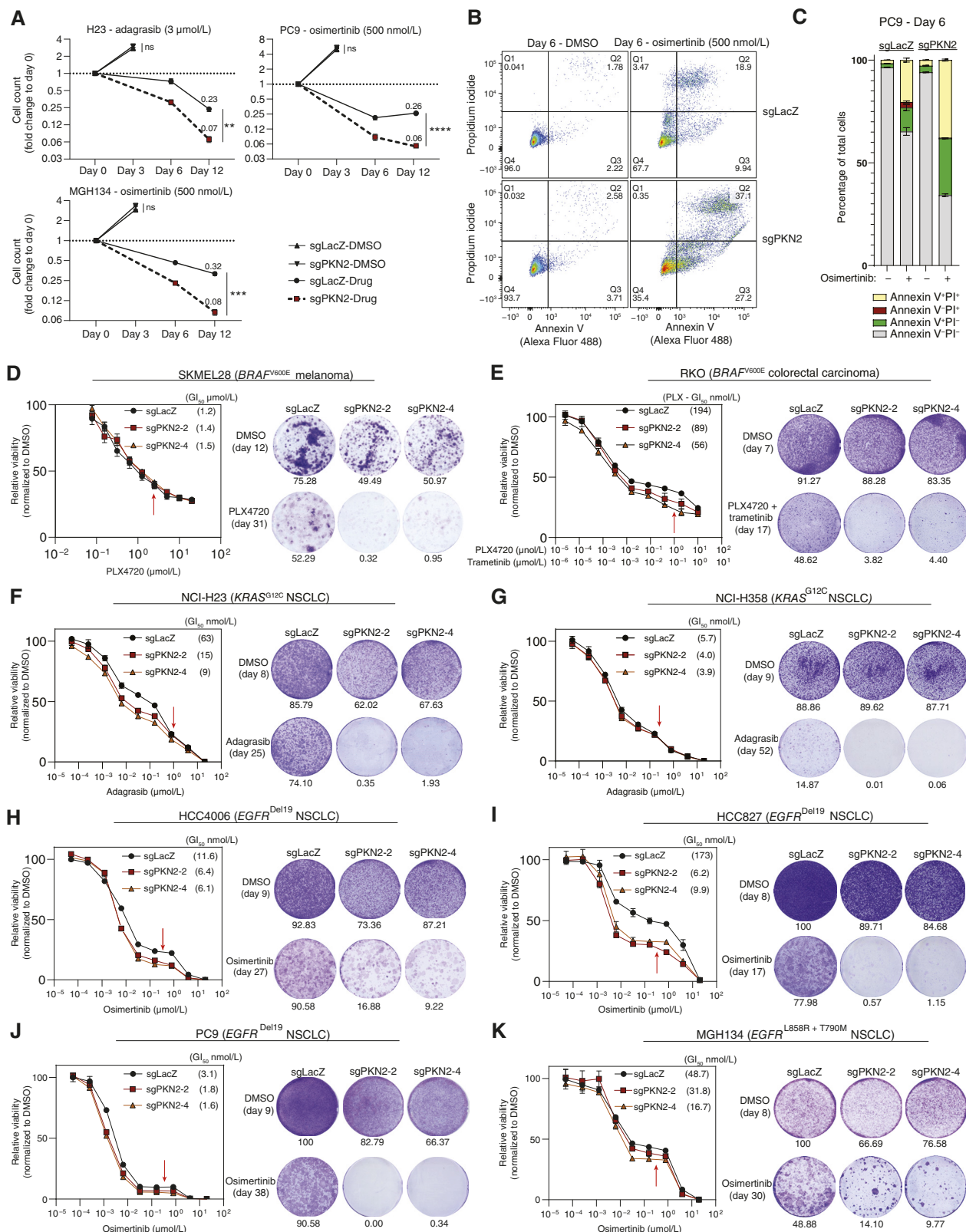


Figure 6. PKN2 inhibition suppresses resistance to oncogene-targeted therapies. **A**, sgLacZ or sgPKN2 NCI-H23, PC9, and MGH134 were subjected to the indicated treatment regimen. Cell counts were taken on day 3 for DMSO-treated groups and on day 6 and day 12 for oncogene-targeted therapy groups. A two-way unpaired t test was performed, and P values are defined as **, $P < 0.01$; ***, $P < 0.001$; ****, $P < 0.0001$. **B**, Cell surface staining of sgLacZ or sgPKN2 PC9 cells with annexin V and propidium iodide (PI) following treatment with 6 days of osimertinib. (continued on following page)

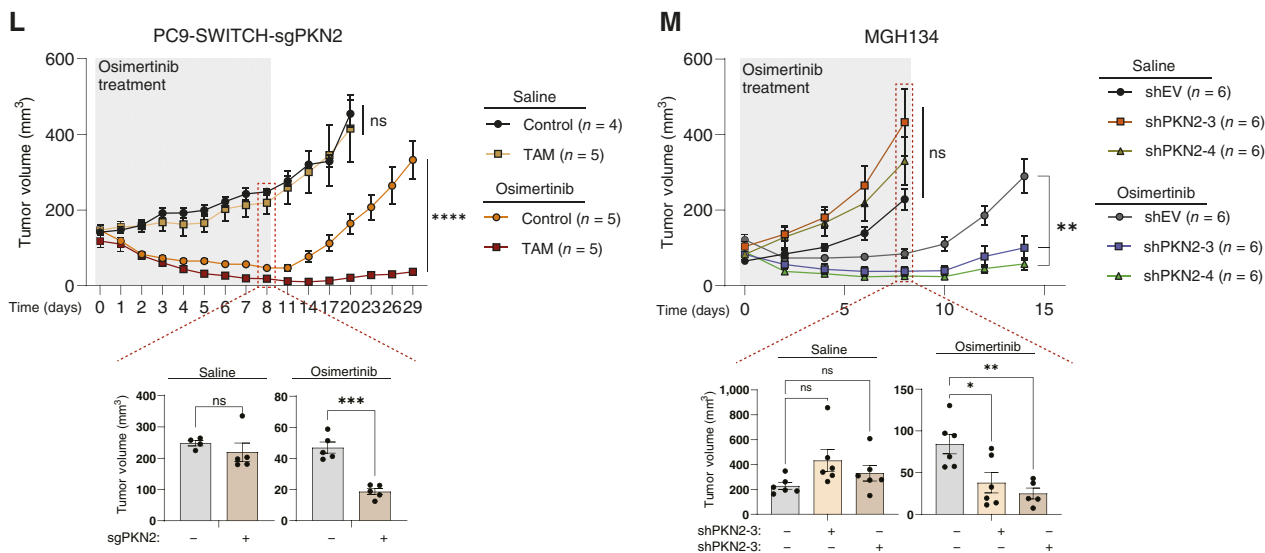


Figure 6. (Continued) Drug was refreshed every 72 hours. **C**, Quantification of biologic triplicates from experiment (B). **D–K**, Left, Short-term dose-response curves: Directly following puromycin selection, the indicated cell lines expressing sgLacZ, sgPKN2-2, or sgPKN2-4 were seeded at 1,000–2,000 cells per well in 96-well plates. The following day, the cells were dosed with the indicated drug series. CellTiter-Glo was performed 72 hours after drugging. GI₅₀ dose is shown in parentheses for each condition. The red line indicates the drug dose used for the long-term resistance assays. **D–K**, Right, Long-term resistance assays: Directly following puromycin selection, the indicated cell lines expressing sgLacZ, sgPKN2-2, or sgPKN2-4 were seeded at 50,000–75,000 cells per well in six-well format. The following day the cells were treated with DMSO or their cognate targeted therapy at the following doses: SKMEL28 (PLX4720—3 μmol/L), RKO (PLX4720—1 μmol/L + trametinib—100 nmol/L), NCI-H23 (adagrasib—1 μmol/L), NCI-H358 (adagrasib—250 nmol/L), HCC4006 (osimertinib—500 nmol/L), HCC827 (osimertinib—500 nmol/L), PC9 (osimertinib—500 nmol/L), and MGH134 (osimertinib—500 nmol/L). All drugs were refreshed every 72 hours. Crystal violet staining was performed when the sgLacZ population hit confluence. **L**, Top, Following PC9-SWITCH-sgPKN2-2 tumor formation, mice were randomly selected to one of the four indicated treatment groups (five mice per group total). The mice were treated with nine daily oral gavages of saline or osimertinib (5 mg/kg). On days 0, 1, and 2, mice were intraperitoneally injected with corn oil (control) or 3 mg of tamoxifen (TAM). Tumor growth kinetics were measured on the indicated days. Two-way ANOVA was performed, and P values for the last day of measurements are defined as ****, P < 0.0001, (bottom) day 8 tumor measurements are highlighted. A two-way unpaired t test was performed, and P values are defined as ***, P < 0.001. **M**, Top, Once MGH134 tumors with the specified doxycycline-inducible hairpins were grown, they were randomly selected to a saline or osimertinib (5 mg/kg) treatment group (six mice per group total). The mice were treated with nine daily oral gavages of saline or osimertinib (5 mg/kg). All mice received daily oral gavages of doxycycline (1 mg) throughout the study. Tumor growth kinetics were measured on the indicated days. Two-way ANOVA was performed, and P values for the last day of measurements are defined as **, P < 0.01, (bottom) day 8 tumor measurements are highlighted. One-way ANOVA was performed, and P values are defined as *, P < 0.05; **, P < 0.01. **A, D–K**, Left, **L–M**, Data are presented as mean ± SEM.

models on day 12 of treatment (Fig. 6A), a finding that was associated with increased apoptotic cell death in these models (Fig. 6B and C).

We next surveyed the effects of upfront *PKN2* knockout on short- and long-term responses to oncogene-targeted therapies. In a 3-day assay, *PKN2* knockout had little to no effect on the sensitivity of eight oncogene-driven cell line models to their cognate targeted therapies, with only two of these models (NCI-H23 and HCC827) exhibiting a greater than fourfold decrease in the dose required to inhibit growth by 50% (GI₅₀; Fig. 6D–K). However, *PKN2* knockout strongly attenuated the long-term expansion of targeted therapy-resistant cells across all surveyed models (Fig. 6D–K). The observation that *PKN2* knockout only modestly affected short-term drug responses but substantially suppressed the abundance of long-term expanded drug-resistant cells is consistent with its ability to deplete mesenchymal-like residual tumor cells.

Interestingly, examination of data from a diverse array of published genome-wide CRISPR knockout screens revealed that *PKN2* knockout cells are selectively depleted in the context of long-term culture with diverse targeted therapies

(Supplementary Fig. S4E; refs. 68, 72–74). Similarly, data from published CRISPR activation screens revealed that *PKN2* overexpression protects cells from long-term treatment with targeted therapies (Supplementary Fig. S4E; ref. 75). Finally, a directed CRISPR knockout screen identified *PKN2* as one of the top genes that, when knocked out, depletes rare BRAF inhibitor-resistant, mesenchymal-like tumor subclones from a melanoma cell population (Supplementary Fig. S4E; ref. 76). These data from independent, unbiased screens support the notion that *PKN2* loss improves the long-term responsiveness of tumor cell populations to oncogene-targeted therapies (Supplementary Fig. S4E).

To evaluate whether *PKN2* regulates the survival of residual cancer cells *in vivo*, we established subcutaneous xenografts of two *EGFR*-mutant NSCLC models in which *PKN2* can be knocked out with CRISPR/Cas9 (PC9-SWITCH-sgPKN2) or knocked down with RNA interference (MGH134-shPKN2; Supplementary Fig. S4F). Using a recently validated protocol, we generated the residual tumor state in these xenograft models with a nine-dose regimen of osimertinib at 5 mg/kg (77). At the start of osimertinib treatment, we induced the knockout of *PKN2* in the PC9 tumors with tamoxifen and

the knockdown of *PKN2* in patient-derived MGH134 tumors with doxycycline. *PKN2* loss did not affect the growth of the saline-treated control tumors but significantly increased the depth of response to osimertinib in both xenograft models by day 8 of drug treatment [Fig. 6L and M (bottom)], as supported by the observation of diminished residual tumor cell outgrowth following drug withdrawal [Fig. 6L and M (top)].

Together, these data suggest that *PKN2* inhibition may be a potent strategy for enhancing the depth and duration of responses to diverse oncogene-targeted therapies.

DISCUSSION

In this study, we discovered that a poorly characterized kinase, *PKN2*, is a top dependency specific to the MLS through an unbiased pan-cancer analysis of ~800 cancer cell lines. We leveraged recent advancements in coessentiality mapping to predict and validate that *PKN2* functions as a negative regulator of the Hippo tumor suppressor pathway and showed that *PKN2* dependence is rescueable through forced expression of a Hippo-resistant TAZ mutant. Mechanistically, we utilized convergent findings from *PKN2*-specific quantitative phosphoproteomics, a kinome-wide atlas of serine/threonine substrates (53), Alphafold3 (56), and kinome interactome studies (55) to discover that *PKN2* exerts its antagonistic effects on Hippo signaling via direct phosphorylation of SAV1^{S90}. Translationally, we observed that *PKN2* kinase activity is enriched in human tumors with a high YAP/TAZ transcriptional signature and mesenchymal-like features through a pan-cancer analysis of CPTAC data (58–60). Finally, we leveraged our mechanistic understanding of *PKN2* dependence for therapeutic benefit, demonstrating that *PKN2* suppression inhibits the survival of mesenchymal-like residual tumor cells following treatment with BRAF/MEK-, EGFR-, and KRAS-targeted therapies.

The findings presented in this study highlight the interwoven relationship between TAZ activation and the MLS (52). Because YAP/TAZ and mesenchymal-like signatures mirror each other across a pan-cancer analysis of cell lines (Supplementary Fig. S2C) and patient tumor samples (Supplementary Fig. S3I), it is no surprise that oncogenic YAP/TAZ activity acts as a core survival program in the MLS (Supplementary Fig. S2E). Notably, our results suggest that TAZ, and not YAP, is functionally crucial for the survival and proliferation of tumor cells in the MLS (Supplementary Fig. S2E and S2F). Furthermore, YAP and TAZ gene dependency scores do not correlate across cancer lineages (Supplementary Fig. S2G), a finding which is in line with recent literature that suggests YAP and TAZ can associate with different DNA-binding partners, resulting in the activation of distinct transcriptional programs and downstream phenotypic outcomes in cancer (78–80). The contextual differences between YAP and TAZ functions in the context of cancer cell survival are poorly understood (47) and will require elucidation before future YAP- or TAZ-specific pharmacologic inhibitors can be rationally applied.

Our pan-cancer analysis identified TAZ and multiple integrin-focal adhesion network members as top MLS dependencies. Induction of the MLS is associated with cytoskeletal

rearrangement and remodeling of the extracellular matrix, which alters extracellular-intracellular communication and downstream signaling events in mesenchymal cells (81). As focal adhesion signaling is known to regulate Hippo signaling through PTK2 (82) and ILK (83), we suspect the increased dependence on the focal adhesion complex in mesenchymal cells is mechanistically linked to its activation of TAZ. Interestingly, focal adhesion and YAP/TAZ signaling are recurrently identified contributors to therapeutic resistance across cancer lineages and drug classes (46, 67, 68, 84, 85). Rather than focal adhesion-Hippo signaling being required for resistance to any specific agent, our work supports a model in which drug resistance broadly selects for a cancer population with mesenchymal-like features that have acquired a convergent dependency on focal adhesion-Hippo signaling for survival. Additionally, because *PKN2* is known to become activated following Rho GTPase binding (86, 87), our discovery provides a potential direct link between focal adhesion and Hippo signaling regulation through RhoA-PKN2 or Rac1-PKN2 interactions (44, 46, 54). Future work will be required to elucidate the upstream activators of *PKN2* in mesenchymal-like cells.

This work identifies *PKN2* as a novel regulator of the Hippo tumor suppressor pathway and the first kinase to antagonize SAV1 function through phosphorylation of S90 in human cells. Phosphorylation of SAV1 on its N-terminus (T26, S36, and S68) is known to break its inhibitory interaction with the protein phosphatase 2A (PP2A) complex STRIPAK^{SLMAP}, which then goes on to dephosphorylate and inactive MST1/2 (48, 88). It is plausible that phosphorylation of SAV1^{S90} inhibits Hippo signaling through the activation of STRIPAK^{SLMAP}, but future signal transduction studies are needed to clarify the precise downstream effects of SAV1^{S90} phosphorylation. Taken together, the high degree of conservation across vertebrate species (Supplementary Fig. S3F), the placement of arginine at the -3, -2, and +2 residue positions (Supplementary Fig. S3F), and the signaling data presented in this study suggest that SAV1^{S90} is a key site for regulatory phosphorylation by basophilic kinases.

Our study finds that *PKN2* primarily exerts its antagonistic effects on Hippo signaling through SAV1^{S90}. However, our findings do not rule out the possibility that additional contributing factors may play a role in *PKN2*'s regulation of Hippo signaling. It is conceivable that *PKN2* may directly phosphorylate additional members of Hippo signaling to exert its full effect (Supplementary Fig. S3D) or that it may additionally inhibit Hippo signaling through indirect signaling events, such as f-actin regulation (89). Although our data suggest that *PKN2*'s regulation of YAP/TAZ is entirely Hippo-dependent, there is evidence that *PKN2* may regulate YAP/TAZ activation through a Hippo-independent mechanism (38). Nonetheless, *PKN2*'s potent regulatory effects on YAP/TAZ suggest it is a core regulator of Hippo signaling in mesenchymal-like cells, which may explain its requirement for mammalian mesoderm expansion in embryogenesis (35).

The results of this work add to an increasing appreciation for the profound role of YAP and TAZ signaling as an oncogenic driver in diverse human cancers, leading to great interest in developing drugs that inhibit its function. Achieving this goal has been challenging, as no known, conventionally

druggable proteins positively regulate YAP/TAZ function within the Hippo pathway. A breakthrough came in recent years with the discovery of a central, cysteine-containing pocket on the TEAD proteins, and their palmitoylation is required for YAP/TAZ binding (90). The first clinical pan-TEAD inhibitor, VT3989, recently showed promising Phase I efficacy and tolerability in YAP-driven mesothelioma patients (NCT04665206), providing the first evidence for targeting YAP/TAZ as an anticancer strategy in patients. Our study proposes PKN2 as an attractive target for pharmacologic inhibition in TAZ-driven cancer contexts, such as BRAFⁱ, EGFRⁱ, and KRASⁱ drug-tolerant residual tumors. As inhibition of PKN2 activates Hippo signaling, leading to the degradation of TAZ, this mechanism is potentially advantageous over TEAD inhibition, which does not block TAZ's transcriptional activity from alternative DNA-binding partners (49, 79). Unfortunately, no specific inhibitors of PKN2 have been characterized yet. However, PKN2 seems to be a prime candidate for pharmacologic inhibition, as its knockout is well tolerated in adult mice (38), chemical probes targeting PKN2 are already created (36, 37), and its kinase activity is enriched in and required for the survival of TAZ-driven mesenchymal-like cancers (Fig. 4).

METHODS

Study Approval

The Institutional Animal Care and Use Committee at Duke University (IACUC) approved all animal procedures and studies. The study's IACUC protocol number is A189-22-11.

Cell Culture

The following cell lines were used: 22rv1 (RRID: CVCL_1045), HCT-15 (RRID: CVCL_0292), MCF-7 (RRID: CVCL_0031), NCI-H1437 (RRID: CVCL_1472), A375 (RRID: CVCL_0132), NCI-H2030 (RRID: CVCL_1517), PC3 (RRID: CVCL_0035), BT549 (RRID: CVCL_1092), SKMEL28 (RRID: CVCL_0526), HEK293-FT (RRID: CVCL_6911), HCC4006 (RRID: CVCL_1269), HCC827 (RRID: CVCL_2063), PC9 (RRID: CVCL_B260), NCI-H23 (RRID: CVCL_1547), NCI-H358 (RRID: CVCL_1559), and RKO (RRID: CVCL_0504). MGH134 (RRID: CVCL_DH54) cells were a gift from Dr. Aaron Hata. All cells were purchased from the ATCC or Duke University Cell Culture Facility and were maintained in a humidified incubator at 37°C with 5% CO₂. Each cell line had short tandem repeat profiling performed at the Duke University DNA Analysis Facility to confirm their authenticity. Cells were never passaged for more than 6 weeks before being discarded. Regular *Mycoplasma* testing with the MycoAlert Mycoplasma Detection Kit (Lonza, # LT07-318) was employed to ensure the cell lines were free from contamination. PC3 cells were cultured in DMEM/F12 (1:1; Gibco), 293FT cells were cultured in DMEM high glucose (Gibco) with 1% nonessential amino acids and 1% sodium pyruvate added, and all other cell lines were cultured in RPMI (Gibco). All media was supplemented with 10% fetal bovine serum (VWR) and 1% penicillin/streptomycin (Gibco).

Chemicals

In vitro. PLX4720, trametinib, osimertinib, and adagrasib were purchased from Selleck Chemicals and prepared at 100 μmol/L stock solutions in DMSO. Doxycycline was purchased from VWR (103516-794) and was prepared at 2 mg/mL in molecular biology-grade water. 4-Hydroxytamoxifen was purchased from MedChem (HY-16950) and prepared in 10 mmol/L stock solutions in DMSO.

Puromycin Dihydrochloride (6136) and G418 Sulfate (G-418-10) were purchased from Gold Biotechnology. Blastocidin S was purchased from Sigma (203351).

In vivo. Doxycycline hydrate 98% (AC446061000) was purchased from Thermo Fisher Scientific. Tamoxifen was purchased from MedChemExpress (HY-13757A). Clinical-grade osimertinib (Tagrisso—AstraZeneca) was purchased from Duke Pharmacy.

Plasmids and Cloning

Plasmids. The following plasmids were purchased from Addgene: lentiCRISPR v2 (LCV2; RRID: Addgene_52961), Tet-pLKO-puro (RRID: Addgene_21915), pRDA_355 (RRID: Addgene_187159), pLenti-EF-FH-TAZ-ires-blast (RRID: Addgene_52083), N174-MCS (RRID: Addgene_81061), HA-sav (RRID: Addgene_32834), pKLV2-EF1a-Cas9Bsd-W (RRID: Addgene_68343), psPAX2 (RRID: Addgene_12260), pMD2.g (RRID: Addgene_12259), pClneoMyc human MST2 (RRID: Addgene_37022), p-EF1a-CreERT2-3Xflag-T2A-eBFP2 (RRID: Addgene_170186), and pcDNA3.1-2xFLAG-2xSTREP (RRID: Addgene_172604). pLVX-TP-3F-TAZ4SA was a gift from Ann Marie Pendergast. pLenti_SWITCH-ON_PGK-Neo was a gift from Ulrich Elling (Institute of Molecular Biotechnology, Austrian Academy of Sciences, Vienna, Austria). PRK2/Prkcl2 cDNA ORF Clone in Cloning Vector, Human was purchased from Sino Biological (HG10536-M).

Restriction Enzyme Cloning. Full-length and Δ642-PKN2 were PCR amplified out of its cloning vector with Q5 High-Fidelity 2X Master Mix (NEB, M0492S) according to the manufacturer's protocols and ligated into pcDNA3.1-2xFLAG-2xSTREP. Additionally, TAZ^{S4A} was amplified out of pLVX-TP-3F-TAZ4SA and ligated into N174-MCS. All resulting plasmids were confirmed with Sanger sequencing.

Site-Directed Mutagenesis. PCR Primers were designed using the Agilent Primer Design tool. PCR was carried out using PfUUltra II FUSion HotStart DNA polymerase (Agilent, 600670) according to the manufacturer's protocol. All resulting point mutations were validated with Sanger sequencing.

DepMap Analyses

All datasets used in this article were from the 23Q4 public data release from Cancer Dependency Map Portal (RRID: SCR_017655) at the Broad Institute.

Lineage-Based Analyses. Using the custom cell line list feature, we separated all cell lines from lymphoid and myeloid lineages, fibroblasts, colorectal adenocarcinoma, breast carcinoma, esophago-gastric cancer, mesothelioma, head and neck squamous, renal cell carcinoma, small cell lung cancer, non-small cell lung cancer, pancreatic adenocarcinoma, ovarian cancer, and melanoma based on their DepMap lineage annotation. We downloaded the DepMap ssGSEA dataset for all lineages and extracted the Hallmark EMT gene set to be used for the EMT score. For PKN2, YAP1, WWTR1, and TEAD1 dependency scores, we downloaded the CRISPR (DepMap Public 23Q4+ Score, Chronos) data for each lineage.

Correlation Analyses. All DepMap correlation analyses were performed in the custom analysis browser using the Pearson correlation analysis. The DepMap ssGSEA Hallmark EMT score was correlated against CRISPR (DepMap Public 23Q4+ Score, Chronos) data in all solid cancer cell lines excluding mesenchymal-derived lineages to generate the Pearson correlation coefficients for our EMT score versus CRISPR gene score analysis. We performed GSEAPrereanked using GSEA v4.2.3 (RRID: SCR_003199) on the ranked list of correlation coefficients with all the Kegg_Legacy v2023.2 curated gene

sets (RRID: SCR_018145). We repeated this analysis using just lung cancer-derived lineages to create the lung cancer-specific EMT score versus CRISPR score Pearson correlation coefficients. The DepMap ssGSEA Hallmark EMT score was correlated against Expression Public 23Q4 data in all solid cancer cell lines, excluding mesenchymal-derived lineages, to generate the Pearson correlation coefficients for our EMT score versus Expression analysis. We downloaded the Expression Public 23Q4 and performed ssGSEA with GenePattern (91) using a YAP/TAZ-specific 22-target gene signature (45) to generate the YAP/TAZ score for every cell line. We correlated the YAP/TAZ score against the EMT score (DepMap ssGSEA) and PKN2 dependency [CRISPR (DepMap Public 23Q4+ Score, Chronos)] using every cell line represented across these datasets.

PKN2 Dependence Predictability. We downloaded the depmap_predictability_data_PKN2 dataset for CRISPR (DepMap Public 23Q4+ Score, Chronos) and RNAi (Achilles+DRIVE+Marcotte, DEMETER2) datasets. Only the Core Omics model data was incorporated into our article.

Coessentiality Mapping

We searched for PKN2 on coessentiality.net, created a list of genes immediately surrounding PKN2, and analyzed this list of genes using Gene Ontology with the Reactome pathways annotation data set. We downloaded the plot of PKN2's "neighborhood" from coessentiality.net and annotated known Hippo pathway members. From DepMap, we downloaded PKN2's top 100 codependencies for CRISPR (DepMap Public 23Q4+Score Chronos) and represented the top 15 genes in a table.

CPTAC Analysis

To generate a YAP/TAZ transcriptional score for each patient represented in the CPTAC pan-cancer data (RRID: SCR_017135), we first downloaded the RNA-seq file "RNA_Broad_v1.zip" from pdc.cancer.gov. We used a 22-gene YAP/TAZ target gene signature (45) and performed ssGSEA on the processed patient RNAseq data with Genepattern (91). Using simple linear regression models in R, we correlated YAP/TAZ score against processed proteome data from "Proteome_Broad_Institute_harmonized_v1" and phosphoproteome data from "Phosphoproteome_Broad_Institute_harmonized_v1". The resulting ranked list of correlation coefficients from YAP/TAZ score versus proteome were further analyzed with GSEAPreranked using Hallmark gene sets. The resulting ranked list of correlation coefficients from the YAP/TAZ score versus phosphoproteomics data was analyzed with GSEAPreranked using kinase substrate signatures generated from the atlas of serine/threonine substrates (53). As recommended by the authors, the kinase substrate signature included all phosphosites in which the given kinase was a top 15-ranked kinase.

CRISPR/Cas9 Knockouts

Constitutively Active System. sgRNAs against the chosen gene were cloned into LCV2 and validated with Sanger sequencing. Lentivirus for each plasmid was generated as previously described (40). Cells were subjected to spinfection with a transduction mixture of virus, 8 µg/mL polybrene, and media at 2,250 rpm for 1 hour. The following day, the media was refreshed, and the cells with plasmid integration were selected with 2 µg/mL puromycin. To select a biallelic knockout clone, we serially diluted our puromycin-selected population to a density of 1 cell/well in a 96-well plate and identified knockout clones through immunoblotting.

Inducible Tet-on-sgRNA System. PC9 and NCI-H23 cells were transduced with lentivirus containing pKLV2-EF1a-Cas9Bsd-W and selected for stable Cas9 expression with 10 µg/mL blasticidin.

sgRNAs against PKN2 were cloned into pRDA_355. PC9-Cas9 and H23-Cas9 cells were transduced with lentivirus containing pRDA_355-sgCTRL or pRDA_355-sgPKN2. Plasmid integration was selected for in tet-free FBS media with 2 µg/mL puromycin. Immunoblot validation of on-target knockout was achieved with 500 ng/mL doxycycline for 96 hours.

All sgRNA sequences were chosen from the TKOv3 genome-wide library (LacZ: CAGCTGGCGTAATAGCGAAG, sgCTRL: GGT GTGCGTATGAAGCAGTG, PKN2-1: TTGTTGCTAGTAGAACACG, PKN2-2: GCAGTTGCTGAGCTGTACCA, PKN2-3: AGTTCAAGAG GACTTATCAC, PKN2-4: ATGGGACCAGAAGTTTACAC, SAV1: TGACACTCACTCCGAAGCAG, WWTR1-1: GAGGAAGTACCTCT GGCCAG, WWTR1-2: ACTGGTGTGGAAGTACGGC, YAP1-1: AAGGCCTGCTGCCCTGGCCC, and YAP1-2: GAATGAGCTCGA ACATGCTG; ref. 92) and were validated for on-target protein loss with immunoblotting.

Clonogenic Growth Assay

We seeded 1,000 to 5,000 cells per well in triplicate in six-well tissue culture plates directly following their puromycin selection to measure the proliferative effects of single gene knockouts in parental cell populations. The cells were grown in standard growth media until the sgLacZ population hit confluence and then were fixed and stained with 0.5% (w/v) crystal violet in 6.0% (v/v) glutaraldehyde (Thermo Fisher Scientific). Quantifications of the surface area covered were used to estimate cell viability and were performed in ImageJ software (RRID: SCR_003070) with the ColonyArea plugin (93).

We seeded 50,000 to 75,000 cells per well in a six-well format for long-term drug resistance experiments. The following day, we started treatment with the indicated pharmacologic inhibitor or DMSO, and the cells were maintained in culture until the sgLacZ population hit confluence. The media and inhibitors were refreshed every 72 hours. The assays were stained and quantified as previously described.

Immunoblotting

Western blot procedure was followed as previously described (94). The following primary antibodies were purchased from Cell Signaling Technology and diluted at 1:1,000: E-cadherin (#3195, RRID: AB_2291471), N-cadherin (13116, RRID: AB_2687616), AXL (#8661, RRID: AB_11217435), vimentin (#5741, RRID: AB_10695459), HSP90 (#4877, RRID: AB_2233307), phospho-PKN2 (T816; #2611, RRID: AB_2268567), PKN2 (#2612, RRID: AB_2167753), LATS1 (#3477, RRID: AB_2133513), phospho-LATS1 (Thr1079; #8654, RRID: AB_10971635), phospho-YAP (Ser397; #13619, RRID: AB_2650554), phospho-YAP (Ser127; #4911, RRID: AB_2218913), YAP/TAZ (#8418, RRID: AB_10950494), β-actin (#4970L, RRID: AB_2223172), HA-Tag (#3724, RRID: AB_1549585), SAV1 (#13301, RRID: AB_2798176), phospho-PKA Substrate (RRXS*/T*; #9624, RRID: AB_331817), and vinculin (#13901, RRID: AB_2728768). M2 FLAG antibody (Sigma-Aldrich, Cat. #F1804, RRID: AB_262044).

SAV1 Immunoprecipitation. 293FTs were transfected with the indicated combination of HA-SAV1, FL-PKN2, and Δ642-PKN2 plasmids at a 1:1 ratio using Lipofectamine 2000. Twenty-four hours after transfection, the cells were lysed with RIPA and incubated with precleared Anti-HA Magnetic Beads (MedChemExpress) overnight at 4°C. The beads were washed multiple times with lysis buffer before being boiled in a 4× Laemmli SDS sample buffer and subject to immunoblotting.

SAV1 Phostag Gel. 293FTs were transfected with the indicated combination of HA-SAV1 mutants, Δ642-PKN2, and Δ642^{K686A}-PKN2 plasmids at a 1:1 ratio using Lipofectamine 2000. Twenty-four hours after transfection, lysates were made as previously described and ran on either a NuPAGE 4% to 12%, Bis-Tris, 1.0- to 1.5-mm gel

(Thermo Fisher Scientific) or a SuperSep Phos-tag (50 μmol/L), 7.5% gel (Fujifilm). The Phostag gel was washed multiple times with EDTA before transferring onto a polyvinylidene difluoride membrane.

In Vitro Kinase Assay

HA-SAV1^{WT} and HA-SAV1^{S90A} plasmids were transfected into 293FT cells for 24 hours before being immunoprecipitated with a HA-bead pulldown, as previously described. Following multiple washes, the HA-beads containing bound SAV1^{WT} or SAV1^{S90A} were resuspended in a 40 μL kinase reaction mixture that contained 0.5 mmol/L ATP (Cell Signaling Technology, #9804), 12.5 nmol/L GST-PKN2 (SignalChem Biotech, P71-10G), 1× Protein Kinase Buffer 9, Cell Signaling Technology, #9802), and ddH₂O. The reaction was carried out at room temperature for 15 minutes. A total of 13.3 μL of NuPAGE LDS Sample Buffer (4x) was added to the reaction mixture and boiled at 95 degrees for 5 minutes. The HA beads were separated with a magnetic stand, and the lysate was transferred to a new Eppendorf before being analyzed with immunoblotting.

RT-qPCR

The TaqMan qPCR protocol was followed as previously described (94). The catalog numbers for the TaqMan probes are as follows: TBP (Hs00427620_m1), ANKRD1 (Hs00173317_m1), CTGF (Hs00170014_m1), CYR61 (Hs00155479_m1), FN1 (Hs01549976_m1), CDH2 (Hs00983056_m1), and VIM (Hs00958111_m1).

Short-term Cell Viability Assays

Cell populations were seeded at 1,000 to 2,000 cells per well in a 96-well plate. The following day, the inhibitor was added at the specified concentrations. Seventy-two hours after adding the drug, the cells were incubated in 10 μL of CellTiter-Glo (Promega) for 10 minutes. The relative cell viability was determined by normalizing the raw luminescence values for each treatment condition to DMSO-treated wells.

Flow Cytometry

Annexin V and Propidium Iodide Staining. Following drug treatment, PC9 cell populations were pelleted and resuspended in a concentration of 1 × 10⁶ cells/mL of 1× annexin-binding buffer. Cells were profiled for cell surface expression of phosphatidylserine with the Dead Cell Apoptosis Kit with Annexin V Alexa Fluor 488 & Propidium Iodide (Invitrogen, # V13245) kit according to the manufacturer's protocol.

Cell-Cycle Analysis. Following drug treatment, Hoechst 33342 (Thermo Fisher Scientific, # 62249) was added to the culture media at 5 μg/mL and incubated at 37°C for 1 hour. Cell populations were collected and resuspended in eBioscience Flow Cytometry Staining Buffer (Thermo Fisher Scientific, # 00-4222-57) at 1 × 10⁶ cells/mL concentration.

Data were acquired with a BD Scientific Canto II Flow Cytometer (RRID: SCR_018056) and the results were analyzed in FlowJo (RRID: SCR_008520).

Quantitative Phosphoproteomics

Sample Preparation. The Duke Proteomics and Metabolomics Core Facility received six samples of 293FT cell pellets (three of each PKN2-Active and PKN2-Dead), kept at -80°C until processing. Samples were supplemented with 100 μL of 8 mol/L urea and subjected to three rounds of sonication at 10 seconds per round. Protein concentrations were determined via Bradford Assay, ranging from 11 to 16 mg/mL. Samples were normalized to 300 μg using 8 mol/L/50 mmol/L ammonium bicarbonate and spiked with undigested casein at a total of either 1 or 2 pmol as an internal quality control standard.

Next, they were supplemented with 4.8 μL of 20% SDS and reduced with 10 mmol/L dithiothreitol for 45 minutes at 32°C, alkylated with 20 mmol/L iodoacamide for 45 minutes at room temperature, and then supplemented with a final concentration of 1.2% phosphoric acid and 283 μL of S-Trap (ProteFi) binding buffer (90% MeOH/100 mmol/L TEAB). Proteins were trapped on the S-Trap mini cartridge, digested using 100 ng/μL sequencing grade trypsin (Promega) for 1.5 hours at 47°C, and eluted using 80 mmol/L TEAB, followed by 0.2% FA, and lastly using 50% ACN/0.2% FA. All samples were then lyophilized to dryness.

Phosphopeptide Enrichment. The phosphopeptide samples were resuspended in 80% acetonitrile and 1% TFA prior to TiO₂ enrichment. Each sample was subjected to complex TiO₂ enrichment (using a competitive modifier) using GL biosciences TiO₂ tips and manufacturer-recommended protocols. Eluted phosphopeptides were then subjected to C18 stage tip cleanup. All samples were frozen and lyophilized to dryness. Samples were resuspended in 12 μL of 1% TFA/2% acetonitrile with 12.5 fmol/μL of yeast ADH and 10 mmol/L citric acid.

LC/MS-MS Analysis. Quantitative LC-MS/MS was performed on 3 μL (25%) of each sample, using an EvoSep One UPLC system coupled to a Thermo Orbitrap Astral high-resolution accurate mass tandem mass spectrometer (Thermo Fisher Scientific) via a nano-electrospray ionization source. The samples were loaded onto the EvoSep tip, and the analytical separation was performed using a 1.5 μm EvoSep 15 cm performance (EvoSep) with a 30 SPD (44 minutes) method. Data collection on the Orbitrap Astral mass spectrometer was performed in a data-independent acquisition (DIA) mode of acquisition with a *r* = 240,000 (@ m/z 200) full MS scan from m/z 380 to 1,080 with a target AGC value of 4e5 ions. Fixed DIA windows of 5 m/z from m/z 380 to 1,080 DIA MS/MS scans were acquired in the Astral with a target AGC value of 5e4 and max fill time of 8 ms. A higher energy collision dissociation setting of 27% was used for all MS2 scans. The total analysis cycle time for each sample injection was approximately 45 minutes.

Quantitative Data Analysis. Following nine total UPLC-MS/MS analyses, data were imported into Spectronaut (Biognosis), and individual LC/MS data files were aligned based on the accurate mass and retention time of detected precursor and fragment ions. Relative peptide abundance was measured based on MS2 fragment ions of selected ion chromatograms of the aligned features across all runs. The MS/MS data was searched against the SwissProt *Homo sapiens* database (downloaded in August 2022), a common contaminant/spiked protein database (bovine albumin, bovine casein, yeast ADH, etc.), and an equal number of reversed-sequence “decoys” for false discovery rate determination. A library-free Spectronaut performs the database searches. Database search parameters included fixed modification on Cys (carbamidomethyl), variable modification on Met (oxidation) and Ser/Thr, and Tyr (phosphorylation). Full trypsin enzyme rules were used along with 10 ppm mass tolerances on precursor ions and 20 ppm on product ion. Spectral annotation was set at a maximum 1% peptide false discovery rate based on *q*-value calculations. Note that peptide homology was addressed using razor rules in which a peptide matched to multiple different proteins was exclusively assigned to the protein with more identified peptides. Protein homology was addressed by grouping proteins that had the same set of peptides to account for their identification. A master protein within a group was assigned based on % coverage.

AlphaFold 3 Prediction

Full-length PKN2 (UniProtKB/Swiss-Prot: Q16513.1) and Full-length SAV1 (UniProtKB/Swiss-Prot: Q9H4B6) sequences were input into AlphaFold 3 using the public server Alphafoldserver.com.

A phosphothreonine PTM was added to full-length PKN2 at residue T816. A phospho-serine PTM was added to full-length SAV1 at residue S90. The resultant protein sequence prediction models were generated on Alphafoldserver.com. The data were processed and annotated in PyMol Version 3.0.3 (RRID: SCR_000305).

In Vivo Experimentation

All mouse experiments were approved by the Duke University IACUC prior to initiation and are in accordance with the Guide for the Care and Use of Laboratory Animals, eighth ed.

Inducible shPKN2 Knockdown Studies. We cloned three PKN2-targeting short-hairpin RNA sequences (1:GCAGGAATTAAATGC ACATATCTCGAGATATGTGCATTAAATTCCCTGC, 3:GCACAT TCATACTGATGTCTCTCGAGAAGACATCAGTATGAATGT GC, 4:GCAGCAGAAATTGGATGATATCTCGAGATATCATC CAATTCTGCTGC) into Tet-pLKO-puro. Lentivirus was prepared with the shRNA plasmids for transduction in PC3, 22rv1, and MGH134 cancer cell lines. We validated PKN2-specific knockdown *in vitro* following treatment with 100 ng/mL doxycycline for 72 hours.

For the prostate models, 6- to 8-week-old male NOD/SCID gamma (NSG) mice were purchased from The Jackson Laboratory and were surgically castrated under anesthesia with proper pain control. One week following castration, 5×10^5 PC3 or 22rv1 shRNA cells were injected into the flanks of the mice in a 1:1 ratio with Matrigel. Once tumors reached 50 to 100 mm³, they were switched to doxycycline water (2 mg/mL) with 5% sucrose.

1×10^6 MGH134 cells containing the appropriate Tet-pLKO-shRNA backbones were subcutaneously injected into 10-week-old female NSG mice flanks in a 1:1 ratio with Matrigel. Once tumors reached 100 mm³, they all began doxycycline treatment and were randomly assigned to a saline or osimertinib treatment group. Osimertinib was resuspended in a sterile solution of 20% Captisol and administered to mice via daily oral gavages at 5 mg/kg for nine total doses. Doxycycline was given via daily oral gavage at 1 mg per mouse for the entirety of the study.

CRISPR-SWITCH Study. PC9 parental cells were transduced with pKLV2-EF1a-Cas9Bsd-W and selected with 5-μg/mL blasticidin for 96 hours. The PC9-Cas9 cells were transduced at an MOI of 0.1 with p-EF1a-CreERT2-3Xflag-T2A-eBFP2, and BFP-expressing cells were sorted into a new population 72 hours later. PC9-Cas9-CreERT2 cells were transduced at a MOI of 0.3 of pLenti_SWITCH-ON_PGK-Neo that contained a cutting control sgRNA sequence (GGTGT GCGTATGAAGCAGTG) or sgPKN2-2 (GCAGTTGCTGAGCTGT ACCA) and were selected for with 500 μg/mL of G418. Following *in vitro* validation of the inducible knockout of PKN2 in PC9-SWITCH-sgPKN2-2 cells, 7.5×10^5 cells were injected into the flanks of 10-week-old female NSG mice 7.5×10^5 in a 1:1 ratio of Matrigel. Once tumors reached 150 mm³, they were randomly assigned to saline-corn oil, saline-tamoxifen, osimertinib-corn oil, and osimertinib-tamoxifen treatment groups. Corn oil or Tamoxifen (3 mg per mouse) dissolved in corn oil was intraperitoneally injected on days 0, 1, and 2 of the study. Osimertinib was resuspended in a sterile solution of 20% Captisol and administered to mice via daily oral gavages at 5 mg/kg for nine total doses.

All tumors were measured via calipers every 1 to 4 days, and tumor volume was calculated $V = (L \times W \times W)/2$ (L = longest diameter and W = shortest diameter). The study continued until IACUC-approved endpoints, including when tumors reached ~1,500 mm³, tumors were ulcerated, or the mice displayed clinical impairments.

Statistical Analysis

All results are shown as means ± SEM unless otherwise shown. P values were determined using unpaired, two-tailed Student *t* tests, or, for grouped analyses, one-way or two-way (ANOVA with the Tukey

post hoc test; $P < 0.05$ was considered statistically significant. Unless otherwise noted, all experiments were performed a minimum of three times, and measurements were taken from individual biological replicate samples.

Data Availability

All data associated with this study are available in the main text or the Supplementary Materials.

Authors' Disclosures

S.T. Killarney reports personal fees for consulting work for Retroviral Therapeutics in an area of biology not relevant to the submitted manuscript. K.C. Wood reports grants from NIH and Department of Defense during the conduct of the study, as well as grants, personal fees, and nonfinancial support from Tavros Therapeutics, nonfinancial support from Celldom, Simple Therapeutics, and Decrypt Biomedicine, personal fees from Retroviral Therapeutics, Guidepoint Global, Bantam Pharmaceuticals, and Apple Tree Partners, and personal fees and nonfinancial support from Stelexis BioSciences outside the submitted work. No disclosures were reported by the other authors.

Authors' Contributions

S.T. Killarney: Conceptualization, data curation, formal analysis, validation, investigation, visualization, methodology, writing—original draft, writing—review and editing. **G. Mesa:** Data curation, validation, investigation, visualization, methodology. **R. Washart:** Data curation, validation, investigation, visualization. **B. Mayo:** Data curation, visualization, methodology. **K. Dillon:** Data curation, validation, methodology. **S.E. Wardell:** Data curation, methodology. **M. Newlin:** Data curation, methodology. **M. Lu:** Data curation, methodology. **A. Abu Rmaileh:** Data curation. **N. Liu:** Data curation. **D.P. McDonnell:** Resources, supervision, investigation, methodology. **A.M. Pendergast:** Resources, supervision, investigation. **K.C. Wood:** Conceptualization, resources, supervision, funding acquisition, investigation, visualization, methodology, writing—original draft, project administration, writing—review and editing.

Acknowledgments

We thank Greg Waitt, Tricia Ho, and Erik J. Soderblom at the Duke Proteomics Core Facility for their generous help in producing the quantitative phosphoproteomics dataset. We thank Aaron Hata (Massachusetts General Hospital) for providing MGH134 cells. This research was supported by Duke University School of Medicine start-up funds and support from the Duke Cancer Institute (K.C. Wood). We thank the NIH awards R01CA263593 (K.C. Wood), R01 CA246133 (A.M. Pendergast), 5P30-CA014236-50 (A.M. Pendergast, K.C. Wood), and F99/K00 CA264162 (B. Mayo); the Department of Defense Lung Cancer Research Program awards W81XWH-21-1-0362 (K.C. Wood) and HT9425-24-1-0338 (K.C. Wood); the Duke Medical Scientist Training Program T32 GM007171 (S.T. Killarney); and the TriCEM Graduate Student Award (S.T. Killarney).

Note

Supplementary data for this article are available at Cancer Discovery Online (<http://cancerdiscovery.aacrjournals.org/>).

Received June 27, 2024; revised October 11, 2024; accepted November 15, 2024; published first November 19, 2024.

REFERENCES

1. Hanahan D. Hallmarks of cancer: new dimensions. *Cancer Discov* 2022;12:31–46.
2. Whiting FJH, Househam J, Baker A-M, Sottoriva A, Graham TA. Phenotypic noise and plasticity in cancer evolution. *Trends Cell Biol* 2024;34:451–64.
3. Kemper K, de Goeje PL, Peepo DS, van Amerongen R. Phenotype switching: tumor cell plasticity as a resistance mechanism and target for therapy. *Cancer Res* 2014;74:5937–41.
4. Marine J-C, Dawson S-J, Dawson MA. Non-genetic mechanisms of therapeutic resistance in cancer. *Nat Rev Cancer* 2020;20:743–56.
5. Gargiulo G, Serresi M, Marine J-C. Cell states in cancer: drivers, passengers, and trailers. *Cancer Discov* 2024;14:610–4.
6. Dongre A, Weinberg RA. New insights into the mechanisms of epithelial-mesenchymal transition and implications for cancer. *Nat Rev Mol Cell Biol* 2019;20:69–84.
7. Haerinck J, Goossens S, Berx G. The epithelial-mesenchymal plasticity landscape: principles of design and mechanisms of regulation. *Nat Rev Genet* 2023;24:590–609.
8. Bakir B, Chiarella AM, Pitarresi JR, Rustgi AK. EMT, MET, plasticity, and tumor metastasis. *Trends Cell Biol* 2020;30:764–76.
9. Dudas J, Ladanyi A, Ingruber J, Steinbichler TB, Riechelmann H. Epithelial to mesenchymal transition: a mechanism that fuels cancer radio/chemoresistance. *Cells* 2020;9:428.
10. Debaugnies M, Rodríguez-Acebes S, Blondeau J, Parent M-A, Zocco M, Song Y, et al. RHOJ controls EMT-associated resistance to chemotherapy. *Nature* 2023;616:168–75.
11. Kim C, Gao R, Sei E, Brandt R, Hartman J, Hatschek T, et al. Chemosensitivity evolution in triple-negative breast cancer delineated by single-cell sequencing. *Cell* 2018;173:879–93.e13.
12. Müller J, Krijgsman O, Tsai J, Robert L, Hugo W, Song C, et al. Low MITF/AXL ratio predicts early resistance to multiple targeted drugs in melanoma. *Nat Commun* 2014;5:5712.
13. Leonetti A, Sharma S, Minari R, Perego P, Giovannetti E, Tiseo M. Resistance mechanisms to osimertinib in EGFR-mutated non-small cell lung cancer. *Br J Cancer* 2019;121:725–37.
14. Woolston A, Khan K, Spain G, Barber LJ, Griffiths B, Gonzalez-Exposito R, et al. Genomic and transcriptomic determinants of therapy resistance and immune landscape evolution during anti-EGFR treatment in colorectal cancer. *Cancer Cell* 2019;36:35–50.e9.
15. Gu Y, Zhang Z, Ten Dijke P. Harnessing epithelial-mesenchymal plasticity to boost cancer immunotherapy. *Cell Mol Immunol* 2023; 20:318–40.
16. Felipe Lima J, Nofech-Mozes S, Bayani J, Bartlett JMS. EMT in breast carcinoma—a review. *J Clin Med* 2016;5:65.
17. Vu T, Datta PK. Regulation of EMT in colorectal cancer: a culprit in metastasis. *Cancers (Basel)* 2017;9:171.
18. Xiao D, He J. Epithelial-mesenchymal transition and lung cancer. *J Thorac Dis* 2010;2:154–9.
19. Papanikolaou S, Vourda A, Syggelos S, Gyftopoulos K. Cell plasticity and prostate cancer: the role of epithelial-mesenchymal transition in tumor progression, invasion, metastasis and cancer therapy resistance. *Cancers (Basel)* 2021;13:2795.
20. Piva F, Giulietti M, Santoni M, Occhipinti G, Scarpelli M, Lopez-Beltran A, et al. Epithelial to mesenchymal transition in renal cell carcinoma: implications for cancer therapy. *Mol Diagn Ther* 2016;20: 111–7.
21. Pedri D, Karras P, Landeloos E, Marine J-C, Rambow F. Epithelial-to-mesenchymal-like transition events in melanoma. *FEBS J* 2022;289: 1352–68.
22. Radhakrishnan K, Truong L, Carmichael CL. An “unexpected” role for EMT transcription factors in hematological development and malignancy. *Front Immunol* 2023;14:1207360.
23. Ito T, Kudoh S, Ichimura T, Fujino K, Hassan WAMA, Udaka N. Small cell lung cancer, an epithelial to mesenchymal transition (EMT)-like cancer: significance of inactive Notch signaling and expression of achaete-scute complex homologue 1. *Hum Cell* 2017;30: 1–10.
24. Ikezono Y, Koga H, Akiba J, Abe M, Yoshida T, Wada F, et al. Pancreatic neuroendocrine tumors and EMT behavior are driven by the CSC marker DCLK1. *Mol Cancer Res* 2017;15:744–52.
25. Gil J, Marques-Pamies M, Valassi E, Serra G, Salinas I, Xifra G, et al. Molecular characterization of epithelial-mesenchymal transition and medical treatment related genes in non-functioning pituitary neuroendocrine tumors. *Front Endocrinol (Lausanne)* 2023;14:1129213.
26. Prieto TG, Baldavira CM, Machado-Rugolo J, Farhat C, Olivieri EHR, de Sá VK, et al. Pulmonary neuroendocrine neoplasms overexpressing epithelial-mesenchymal transition mechanical barriers genes lack immune-suppressive response and present an increased risk of metastasis. *Front Oncol* 2021;11:645623.
27. Debnath P, Huirem RS, Dutta P, Palchaudhuri S. Epithelial-mesenchymal transition and its transcription factors. *Biosci Rep* 2022;42:BSR20211754.
28. Viswanathan VS, Ryan MJ, Dhruv HD, Gill S, Eichhoff OM, Seashore-Ludlow B, et al. Dependency of a therapy-resistant state of cancer cells on a lipid peroxidase pathway. *Nature* 2017;547:453–7.
29. Hangauer MJ, Viswanathan VS, Ryan MJ, Bole D, Eaton JK, Matov A, et al. Drug-tolerant persister cancer cells are vulnerable to GPX4 inhibition. *Nature* 2017;551:247–50.
30. Zhang C, Liu X, Jin S, Chen Y, Guo R. Ferroptosis in cancer therapy: a novel approach to reversing drug resistance. *Mol Cancer* 2022;21:47.
31. Tsherniak A, Vazquez F, Montgomery PG, Weir BA, Kryukov G, Cowley GS, et al. Defining a cancer dependency map. *Cell* 2017;170: 564–76.e16.
32. Liberzon A, Birger C, Thorvaldsdóttir H, Ghandi M, Mesirov JP, Tamayo P. The Molecular Signatures Database (MSigDB) hallmark gene set collection. *Cell Syst* 2015;1:417–25.
33. Subramanian A, Tamayo P, Mootha VK, Mukherjee S, Ebert BL, Gillette MA, et al. Gene set enrichment analysis: a knowledge-based approach for interpreting genome-wide expression profiles. *Proc Natl Acad Sci U S A* 2005;102:15545–50.
34. Sophocleous G, Owen D, Mott HR. The structure and function of protein kinase C-related kinases (PRKs). *Biochem Soc Trans* 2021;49: 217–35.
35. Quétier I, Marshall JJT, Spencer-Dene B, Lachmann S, Casamassima A, Franco C, et al. Knockout of the PKN family of Rho effector kinases reveals a non-redundant role for PKN2 in developmental mesoderm expansion. *Cell Rep* 2016;14:440–8.
36. Scott F, Fala AM, Takarada JE, Ficu MP, Pennicott LE, Reuillon TD, et al. Development of dihydropyrrolopyridinone-based PKN2/PRK2 chemical tools to enable drug discovery. *Bioorg Med Chem Lett* 2022;60:128588.
37. Arang N, Lubrano S, Ceribelli M, Rigiraccioli DC, Saddawi-Konefka R, Faraji F, et al. High-throughput chemogenetic drug screening reveals PKC-RhoA/PKN as a targetable signaling vulnerability in GNAQ-driven uveal melanoma. *Cell Rep Med* 2023;4:101244.
38. Murray ER, Menezes S, Henry JC, Williams JL, Alba-Castellón L, Baskaran P, et al. Disruption of pancreatic stellate cell myofibroblast phenotype promotes pancreatic tumor invasion. *Cell Rep* 2022;38: 110227.
39. Mani SA, Guo W, Liao M-J, Eaton EN, Ayyanan A, Zhou AY, et al. The epithelial-mesenchymal transition generates cells with properties of stem cells. *Cell* 2008;133:704–15.
40. Maltais J, Killarney ST, Singleton KR, Strobl MAR, Washart R, Wood KC, et al. Drug dependence in cancer is exploitable by optimally constructed treatment holidays. *Nat Ecol Evol* 2024;8:147–62.
41. Wainberg M, Kamber RA, Balsubramani A, Meyers RM, Sinnott-Armstrong N, Hornburg D, et al. A genome-wide atlas of co-essential modules assigns function to uncharacterized genes. *Nat Genet* 2021; 53:638–49.
42. Arnold PK, Jackson BT, Paras KI, Brunner JS, Hart ML, Newsom OJ, et al. A non-canonical tricarboxylic acid cycle underlies cellular identity. *Nature* 2022;603:477–81.
43. Cervia LD, Shibue T, Borah AA, Gaeta B, He L, Leung L, et al. A ubiquitination cascade regulating the integrated stress response and survival in carcinomas. *Cancer Discov* 2023;13:766–95.

44. Calses PC, Crawford JJ, Lill JR, Dey A. Hippo pathway in cancer: aberrant regulation and therapeutic opportunities. *Trends Cancer* 2019;5:297–307.
45. Wang Y, Xu X, Maglic D, Dill MT, Mojumdar K, Ng PK-S, et al. Comprehensive molecular characterization of the Hippo signaling pathway in cancer. *Cell Rep* 2018;25:1304–17.e5.
46. Franklin JM, Wu Z, Guan K-L. Insights into recent findings and clinical application of YAP and TAZ in cancer. *Nat Rev Cancer* 2023;23:512–25.
47. Thrash HL, Pendergast AM. Multi-functional regulation by YAP/TAZ signaling networks in tumor progression and metastasis. *Cancers (Basel)* 2023;15:4701.
48. Bae SJ, Ni L, Osinski A, Tomchick DR, Brautigam CA, Luo X. SAV1 promotes Hippo kinase activation through antagonizing the PP2A phosphatase STRIPAK. *Elife* 2017;6:e30278.
49. Kim M-K, Jang J-W, Bae S-C. DNA binding partners of YAP/TAZ. *BMB Rep* 2018;51:126–33.
50. Barbie DA, Tamayo P, Boehm JS, Kim SY, Moody SE, Dunn IF, et al. Systematic RNA interference reveals that oncogenic KRAS-driven cancers require TBK1. *Nature* 2009;462:108–12.
51. Bauer AF, Sonzogni S, Meyer L, Zeuzem S, Piiper A, Biondi RM, et al. Regulation of protein kinase C-related protein kinase 2 (PRK2) by an intermolecular PRK2-PRK2 interaction mediated by its N-terminal domain. *J Biol Chem* 2012;287:20590–602.
52. Lei Q-Y, Zhang H, Zhao B, Zha Z-Y, Bai F, Pei X-H, et al. TAZ promotes cell proliferation and epithelial-mesenchymal transition and is inhibited by the Hippo pathway. *Mol Cell Biol* 2008;28:2426–36.
53. Johnson JL, Yaron TM, Huntsman EM, Kerelsky A, Song J, Regev A, et al. An atlas of substrate specificities for the human serine/threonine kinaseome. *Nature* 2023;613:759–66.
54. Plouffe SW, Meng Z, Lin KC, Lin B, Hong AW, Chun JV, et al. Characterization of Hippo pathway components by gene inactivation. *Mol Cell* 2016;64:993–1008.
55. Golkowski M, Lius A, Sapre T, Lau H-T, Moreno T, Maly DJ, et al. Multiplexed kinase interactome profiling quantifies cellular network activity and plasticity. *Mol Cell* 2023;83:803–18.e8.
56. Abramson J, Adler J, Dunger J, Evans R, Green T, Pritzel A, et al. Accurate structure prediction of biomolecular interactions with AlphaFold 3. *Nature* 2024;630:493–500.
57. Camacho C, Coulouris G, Avagyan V, Ma N, Papadopoulos J, Bealer K, et al. BLAST+: architecture and applications. *BMC Bioinformatics* 2009;10:421.
58. Geffen Y, Anand S, Akiyama Y, Yaron TM, Song Y, Johnson JL, et al. Pan-cancer analysis of post-translational modifications reveals shared patterns of protein regulation. *Cell* 2023;186:3945–67.e26.
59. Li Y, Porta-Pardo E, Tokheim C, Bailey MH, Yaron TM, Stathias V, et al. Pan-cancer proteogenomics connects oncogenic drivers to functional states. *Cell* 2023;186:3921–44.e25.
60. Li Y, Dou Y, Da Veiga Leprevost F, Geffen Y, Calinawan AP, Aguet F, et al. Proteogenomic data and resources for pan-cancer analysis. *Cancer Cell* 2023;41:P1397–406.
61. Shen S, Vagner S, Robert C. Persistent cancer cells: the deadly survivors. *Cell* 2020;183:860–74.
62. Killarney ST, Tait SWG, Green DR, Wood KC. Sublethal engagement of apoptotic pathways in residual cancer. *Trends Cell Biol* 2024;34:225–38.
63. Lin L, Sabnis AJ, Chan E, Olivas V, Cade L, Pazarentzos E, et al. The Hippo effector YAP promotes resistance to RAF- and MEK-targeted cancer therapies. *Nat Genet* 2015;47:250–6.
64. Hata AN, Niederst MJ, Archibald HL, Gomez-Caraballo M, Siddiqui FM, Mulvey HE, et al. Tumor cells can follow distinct evolutionary paths to become resistant to epidermal growth factor receptor inhibition. *Nat Med* 2016;22:262–9.
65. Shao DD, Xue W, Krall EB, Bhutkar A, Piccioni F, Wang X, et al. KRAS and YAP1 converge to regulate EMT and tumor survival. *Cell* 2014;158:171–84.
66. Kurppa KJ, Liu Y, To C, Zhang T, Fan M, Vajdi A, et al. Treatment-induced tumor dormancy through YAP-mediated transcriptional reprogramming of the apoptotic pathway. *Cancer Cell* 2020;37:104–22.e12.
67. Haderk F, Chou Y-T, Cech L, Fernández-Méndez C, Yu J, Olivas V, et al. Focal adhesion kinase-YAP signaling axis drives drug-tolerant persister cells and residual disease in lung cancer. *Nat Commun* 2024;15:3741.
68. Tiedt R, King FJ, Stamm C, Niederst MJ, Delach S, Zumstein-Mecker S, et al. Integrated CRISPR screening and drug profiling identifies combination opportunities for EGFR, ALK, and BRAF/MEK inhibitors. *Cell Rep* 2023;42:112297.
69. Hagenbeek TJ, Zbieg JR, Hafner M, Mroue R, Lacap JA, Sodir NM, et al. An allosteric pan-TEAD inhibitor blocks oncogenic YAP/TAZ signaling and overcomes KRAS G12C inhibitor resistance. *Nat Cancer* 2023;4:812–28.
70. Kim MH, Kim J, Hong H, Lee S-H, Lee J-K, Jung E, et al. Actin remodeling confers BRAF inhibitor resistance to melanoma cells through YAP/TAZ activation. *EMBO J* 2016;35:462–78.
71. Chylinski K, Hubmann M, Hanna RE, Yanchus C, Michlits G, Uijttewaal ECH, et al. CRISPR-switch regulates sgRNA activity by Cre recombination for sequential editing of two loci. *Nat Commun* 2019;10:5454.
72. Zeng H, Castillo-Cabrera J, Manser M, Lu B, Yang Z, Strande V, et al. Genome-wide CRISPR screening reveals genetic modifiers of mutant EGFR dependence in human NSCLC. *Elife* 2019;8:e50223.
73. Lou K, Steri V, Ge AY, Hwang YC, Yogodzinski CH, Shkedi AR, et al. KRASG12C inhibition produces a driver-limited state revealing collateral dependencies. *Sci Signal* 2019;12:eaaw9450.
74. Mukhopadhyay S, Huang H-Y, Lin Z, Ranieri M, Li S, Sahu S, et al. Genome-wide CRISPR screens identify multiple synthetic lethal targets that enhance KRASG12C inhibitor efficacy. *Cancer Res* 2023;83:4095–111.
75. Pfeifer M, Brammell JS, Price S, Pilling J, Bhavsar D, Farcas A, et al. Genome-wide CRISPR screens identify the YAP/TEAD axis as a driver of persister cells in EGFR mutant lung cancer. *Commun Biol* 2024;7:497.
76. Torre EA, Arai E, Bayatpour S, Jiang CL, Beck LE, Emert BL, et al. Genetic screening for single-cell variability modulators driving therapy resistance. *Nat Genet* 2021;53:76–85.
77. Nie M, Chen N, Pang H, Jiang T, Jiang W, Tian P, et al. Targeting acetylcholine signaling modulates persistent drug tolerance in EGFR-mutant lung cancer and impedes tumor relapse. *J Clin Invest* 2022;132:e160152.
78. Plouffe SW, Lin KC, Moore JL III, Tan FE, Ma S, Ye Z, et al. The Hippo pathway effector proteins YAP and TAZ have both distinct and overlapping functions in the cell. *J Biol Chem* 2018;293:11230–40.
79. Reggiani F, Gobbi G, Ciarrocchi A, Sancisi V. YAP and TAZ are not identical twins. *Trends Biochem Sci* 2021;46:154–68.
80. Shreber-Shaked M, Dassa B, Sinha S, Di Agostino S, Azuri I, Mukherjee S, et al. A division of labor between YAP and TAZ in non-small cell lung cancer. *Cancer Res* 2020;80:4145–57.
81. Lamouille S, Xu J, Deryck R. Molecular mechanisms of epithelial-mesenchymal transition. *Nat Rev Mol Cell Biol* 2014;15:178–96.
82. Rausch V, Hansen CG. The Hippo pathway, YAP/TAZ, and the plasma membrane. *Trends Cell Biol* 2020;30:32–48.
83. Serrano I, McDonald PC, Lock F, Muller WJ, Dedhar S. Inactivation of the Hippo tumour suppressor pathway by integrin-linked kinase. *Nat Commun* 2013;4:2976.
84. Diaz Osterman CJ, Ozmadenci D, Kleinschmidt EG, Taylor KN, Barrie AM, Jiang S, et al. FAK activity sustains intrinsic and acquired ovarian cancer resistance to platinum chemotherapy. *Elife* 2019;8:e47327.
85. Mohanty A, Nam A, Srivastava S, Jones J, Lomenick B, Singhal SS, et al. Acquired resistance to KRAS G12C small-molecule inhibitors via genetic/nongenetic mechanisms in lung cancer. *Sci Adv* 2023;9:eade3816.
86. Vincent S, Settleman J. The PRK2 kinase is a potential effector target of both Rho and rac GTPases and regulates actin cytoskeletal organization. *Mol Cell Biol* 1997;17:2247–56.

87. Hutchinson CL, Lowe PN, McLaughlin SH, Mott HR, Owen D. Differential binding of RhoA, RhoB, and RhoC to protein kinase C-related kinase (PRK) isoforms PRK1, PRK2, and PRK3: PRKs have the highest affinity for RhoB. *Biochemistry* 2013;52:7999–8011.
88. Bae SJ, Ni L, Luo X. STK25 suppresses Hippo signaling by regulating SAV1-STRIPAK antagonism. *Elife* 2020;9:e54863.
89. Aragona M, Panciera T, Manfrin A, Giulitti S, Michielin F, Elvassore N, et al. A mechanical checkpoint controls multicellular growth through YAP/TAZ regulation by actin-processing factors. *Cell* 2013;154:1047–59.
90. Pobbatı AV, Kumar R, Rubin BP, Hong W. Therapeutic targeting of TEAD transcription factors in cancer. *Trends Biochem Sci* 2023;48:450–62.
91. Reich M, Liefeld T, Gould J, Lerner J, Tamayo P, Mesirov JP. GenePattern 2.0. *Nat Genet* 2006;38:500–1.
92. Harr T, Tong AHY, Chan K, Van Leeuwen J, Seetharaman A, Aregger M, et al. Evaluation and design of genome-wide CRISPR/SpCas9 knockout screens. *G3 (Bethesda)* 2017;7:2719–27.
93. Guzmán C, Bagga M, Kaur A, Westermarck J, Abankwa D. ColonyArea: an ImageJ plugin to automatically quantify colony formation in clonogenic assays. *PLoS One* 2014;9:e92444.
94. Killarney ST, Washart R, Soderquist RS, Hoj JP, Lebhar J, Lin KH, et al. Executioner caspases restrict mitochondrial RNA-driven type I IFN induction during chemotherapy-induced apoptosis. *Nat Commun* 2023;14:1399.